

# A finite-volume module for cloud-resolving simulations of global atmospheric flows

Piotr K. Smolarkiewicz<sup>a</sup>, Christian Kühnlein<sup>a</sup>,  
Wojciech W. Grabowski<sup>b</sup>,

<sup>a</sup>*European Centre For Medium-Range Weather Forecasts, Reading, RG2 9AX, UK*

<sup>b</sup>*National Center for Atmospheric Research, Boulder, Colorado, 80307, USA*

---

## Abstract

The paper extends to moist-precipitating dynamics a recently documented high-performance finite-volume module (FVM) for simulating global all-scale atmospheric flows [Smolarkiewicz et al., *J. Comput. Phys.* (2016) doi:10.1016/j.jcp.2016.03.015]. The thrust of the paper is a seamless coupling of the conservation laws for moist variables engendered by cloud physics with the semi-implicit, non-oscillatory forward-in-time integrators proven for dry dynamics of FVM. The representation of the water substance and the associated processes in weather and climate models can vary widely in formulation details and complexity levels. The representation adopted for this paper assumes a canonical “warm-rain” bulk microphysics parametrization, recognised for its minimal physical intricacy while accounting for the essential mathematical complexity of cloud-resolving models. A key feature of the presented numerical approach is global conservation of the water substance to machine precision—implied by the local conservativeness and positivity preservation of the numerics—for all water species including water vapour, cloud water, and precipitation. The moist formulation assumes the compressible Euler equations as default, but includes reduced anelastic equations as an option. The theoretical considerations are illustrated with a benchmark simulation of a tornadic thunderstorm on a reduced size planet, supported with a series of numerical experiments addressing the accuracy of the associated water budget.

*Key words:* atmospheric models, cloud resolving models, non-oscillatory forward-in-time schemes, process coupling, numerical weather prediction, climate  
*PACS:*

---

\* Corresponding Author.

*Email address:* smolar@ecmwf.int (Piotr K. Smolarkiewicz).

# 1 INTRODUCTION

A recent article [62] documented the development of a global nonhydrostatic finite-volume module (FVM) designed to enhance an established spectral-transform based numerical weather prediction (NWP) model. FVM adheres to NWP standards, with formulation of the governing equations based on the classical meteorological latitude-longitude spherical framework (§7.2 in [10]). From the perspective of numerical methods, the work [62] synthesised finite-difference [37] and flexible finite-volume [66] discretisations of the computational space. The computational space underlies a generalised curvilinear coordinate representation of the nonhydrostatic PDEs [61] governing global atmospheric dynamics in FVM. Flexible unstructured discretisation in the horizontal circumvents the efficiency issues due to meridians' convergence towards the poles, by resolving the spherical surface with comparable-in-size control volumes in the physical space [66]. The structured finite-difference discretisation in the vertical empowers direct preconditioning of complex elliptic boundary value problems for thin spherical shells of the Earth's atmosphere. Benefits of continuous mappings include the analytic representation of spherical shells with irregular lower boundary [74], mesh adaptivity [37,28], pliancy of physical vertical coordinate [73,66], and minimal overhead of the parallelisation.

Accounting for multiphase thermodynamics due to the ubiquity of water substance in the Earth atmosphere adds substantial complexity to the prognostic equations of the dry dynamics. Generally, the way in which moist processes are represented in atmospheric models depends on the focus of interest and its associated spatio-temporal scale. Such interests can vary from representing the evolution of individual hydrometeors or their particle-number distributions [23,1] to scale-dependent parametrisations accounting only for bulk properties of various phases of water on scales  $\mathcal{O}(10^0)$  m and above [1,15,16]. Here we aim at cloud-resolving simulation of global flows, and employ the bulk cloud microphysics of [15] for parametrising moist-precipitating thermodynamics. It provides a convenient vehicle for the discussion of numerics, while being extendible straightforwardly to more complex schemes; see [17] for a discussion.

The complexity of bulk microphysics is still substantial, even though greatly reduced compared to capturing individual hydrometeors or their particle-number distributions. The density of the moist air depends not only on the pressure and temperature but also on the mass of water vapour carried by the flow. Furthermore, while the water-substance phase transitions directly affect the mass of water vapour, pressure and temperature also vary due to the accompanying latent heating effects. In consequence, the mass continuity equation for moist air includes contributions due to water substance, implying associated mathematical complexity for the resulting conservation laws of

the moist dynamics [72]. To avoid such intricacies, the dry air density can be used in formulating the moist model dependent variables and their governing equations [3]. Then, the water vapour and condensed phase are represented by the mixing ratios; that is, the density ratios of individual water species—e.g., water vapour, cloud water, rain, snow—and dry air. The justification of this continuum model for the condensed phase, as opposed to the multiphase model, is that typical sizes of cloud and precipitation particles are comparable to the Kolmogorov microscale  $\mathcal{O}(10^{-3})$  m for the atmospheric turbulence. Cloud, weather and climate models are typically run with grid lengths at least five orders of magnitude larger than the Kolmogorov microscale and under favourable conditions contain at least  $10^6$  cloud or precipitation particles per grid-box volume. At the same time, the water vapour and condensed phase constitute only a small fraction of the mass of a moist cloudy volume, usually less than 1%. It follows that the impact of moisture on the air heat capacity and other thermodynamic properties — e.g., thermal conductivity, air viscosity, and speed of sound — is then negligible so the relevant thermodynamic parameters (generally functions of state), such as specific heats at constant pressure or volume, can be approximated with these for the dry air; cf. §13.1 in [39]. Furthermore, water substance variables and latent heating due to phase changes enter the dynamics of moist air primarily through the buoyancy term in the vertical momentum equation, in the spirit of the Boussinesq approximation; cf. [32] for a discussion.

Time scales involved in moist atmospheric processes vary wildly. Formation and growth of cloud droplets is practically instantaneous, with time scales between fraction of a second to a few seconds; see [18] and references therein. Warm clouds that feature temperatures above freezing are typically close to water saturation, and this provides a powerful approach to model condensation. Formation and growth of rain through collision/coalescence involves time scales of  $\mathcal{O}(10^3)$  s, much longer than typical time steps in cloud-resolving models, and even longer time scales are involved with ice processes [18]. These physical properties inspire a bespoke strategy to effectively solve the governing equations as discussed in this paper. Depending on the mathematical representation of moist processes, there are corresponding numerical issues to be addressed. For bulk parametrisations common in cloud-resolving models such issues include sign-preservation of water species mixing ratios or monotonicity of relative humidity [49,13] as well as computational efficacy and conservation [14,17].

There are other ways to represent moist thermodynamics, arguably more intuitive than the one discussed here [33]. They are based on the so-called invariant variables such as the total water and the liquid-water potential temperature for the condensation/evaporation alone (cf. [13] and references therein), or the total water and equivalent potential temperature for the condensation/evaporation and warm-rain precipitation (i.e., no ice)—to name a few.

Their underlying methodologies also can be extended for modelling ice-bearing precipitating clouds [71]. Technically, such methods transform the governing equations to derive variables conserved along flow trajectories—in the spirit of the Riemann invariants conserved along the characteristic curves of the governing PDEs (§5.3.1 in [7]). When possible, advecting invariant variables provides simple means for estimating the thermodynamic state of displaced parcels. Because of this, however, the method is inherently explicit, and at odds with the large-time-step semi-implicit time integration schemes at the heart of the flexible all-scale approach documented herein.

The paper is organised as follows. Section 2 extends the governing equations of FVM to moist-precipitating dynamics. The related numerical procedures are spread over sections 3 and 4, from which §3 details the methods for moist-precipitating thermodynamics in the context of an isolated fluid parcel, whereas §4 focuses on coupling this parcel model (*PCM*) with global dynamics. Section 5 substantiates technical developments of the preceding sections, demonstrating the efficacy of the moist FVM with simulation of an idealised supercell thunderstorm on a reduced size planet, a select moist benchmark at cloud-resolving scales. Section 6 concludes the paper.

## 2 ANALYTIC FORMULATION

### 2.1 *Physical contents*

#### 2.1.1 *Governing equations*

The generalised PDEs of FVM assume the compressible Euler equations under gravity on a rotating sphere as default, but include reduced soundproof equations [62] as an option. Here, we focus on the most general case of the compressible Euler equations.<sup>1</sup> Because inclusion of moist processes substantially increases the complexity of the FVM formulation, we proceed gradually and start the presentation with the physically more intuitive advective form of the governing equations formulated in a Cartesian reference frame, representative of cloud models, and introduce the corresponding conservation forms implemented in FVM afterwards in Section 2.2. The advective form of the equations for density of dry air  $\rho$ , velocity vector  $\mathbf{u}$ , potential temperature  $\theta$ , and mixing ratios<sup>2</sup> of water vapour  $q_v$ , cloud water  $q_c$ , and precipitation  $q_p$

---

<sup>1</sup> The reader interested in relative performance of soundproof and compressible equations is referred to [61,31,32] for extended discussions.

<sup>2</sup> The mixing ratio of a given phase of water substance is defined as a ratio of the density of that phase to the density of dry air.

are respectively written as

$$\frac{d\rho}{dt} = -\rho\nabla \cdot \mathbf{u} , \quad (1a)$$

$$\frac{d\mathbf{u}}{dt} = -\frac{\theta(1+q_v/\epsilon)}{\theta_0(1+q_v+q_c+q_p)}\nabla\varphi - \frac{\mathbf{g}}{\theta_a}(\theta' + \theta_a(\varepsilon q'_v - q_c - q_p)) + \mathbf{D} , \quad (1b)$$

$$\frac{d\theta'}{dt} = -\mathbf{u} \cdot \nabla\theta_a + \frac{L\theta}{c_p T}(C_d + E_p) + \mathcal{H} , \quad (1c)$$

$$\frac{dq_v}{dt} = -C_d - E_p + D^{qv} , \quad (1d)$$

$$\frac{dq_c}{dt} = C_d - A_p - C_p + D^{qc} , \quad (1e)$$

$$\frac{dq_p}{dt} = A_p + C_p + E_p + D^{qp} - \frac{1}{\rho}\nabla \cdot (\rho\mathbf{u}_\downarrow q_p) . \quad (1f)$$

On the rhs of (1b),  $\mathbf{g} = (0, 0, -g)$  is the gravitational acceleration (with magnitude  $g$  generally diminishing in radial direction as  $\propto r^{-2}$  [59]), and  $\mathbf{D}$  symbolises momentum dissipation, typically expressed as a divergence of the eddy-stress tensor; whereas  $\mathcal{H}$  in (1c) symbolises a heat source/sink, including eddy diffusion. The primes mark perturbations from an arbitrary stationary moist ambient state, hereafter marked with the subscript  $a$ , assumed to be a known equilibrium solution of the governing PDEs; while the subscript 0 denotes constant reference values. The meaning of the symbols related to the water substance will be explained shortly.

The prognostic equations (1) are supplied with a select form of the gas law

$$\varphi = c_p\theta_0 \left[ \left( \frac{R_d}{p_0} \rho\theta(1+q_v/\epsilon) \right)^{R_d/c_v} - \pi_a \right] , \quad (2)$$

that relates pressure perturbations  $\varphi := c_p\theta_0\pi'$ , with  $\pi' = \pi - \pi_a$  denoting the perturbation of Exner pressure  $\pi = (p/p_0)^{R_d/c_p} = T/\theta$ , to thermodynamic constituents of moist air [3,31]. Here,  $T$  is the temperature,  $R_d = 3.5c_p$  is the gas constant of the dry air,  $\epsilon := R_d/R_v \approx 0.622$  is a ratio of gas constants of dry air and water vapour,  $\varepsilon = 1/\epsilon - 1$ , and  $c_p$  is the specific heat at constant pressure. Noteworthy is the advective form of (2)

$$\frac{d\varphi}{dt} = \xi\phi\nabla \cdot \mathbf{u} - \mathbf{u} \cdot \nabla\phi_a + \xi\phi \left( \frac{\mathcal{R}^\theta}{\theta} + \frac{\mathcal{R}^{qv}/\epsilon}{1+q_v/\epsilon} \right) , \quad (3)$$

where  $\xi := R_d/c_v$ ,  $\phi = \varphi + \phi_a$ ,  $\phi_a = c_p\theta_0\pi_a(\mathbf{x})$ , and  $\mathcal{R}^\theta \equiv \text{RHS}(1c) + \mathbf{u} \cdot \nabla\theta_a$  symbolises cumulative latent and sensible heat sinks/sources on the rhs of (1c) while  $\mathcal{R}^{qv}$  marks the rhs forcing in (1d).

### 2.1.2 Significance of moist variables

Up to this point the presentation addressed the core fluid dynamics aspect of the governing PDEs, with a brief mention of their apparent modifications due to the presence of moisture. For the sake of clarity, here we continue the discussion of the governing PDEs (1) with emphasis on the moist variables in the frame of a single fluid parcel under prescribed ambient conditions—a classical approach in cloud physics [4,33].

Noting that the total water mixing ratio  $q_t$ —in the coefficient of the pressure gradient term in (1b)—is defined as  $q_t := q_v + q_c + q_p$ , it is easy to deduce that  $q_t$  satisfies

$$\frac{dq_t}{dt} = -\frac{1}{\rho} \nabla \cdot (\rho \mathbf{u}_\downarrow q_p) + D^{q_t} , \quad (4)$$

given, say, a common diffusivity  $K_q$  for all  $D^{q_{\dots}} = (1/\rho) \nabla \cdot (\rho K_q \nabla q_{\dots})$  terms. Furthermore, defining the liquid water mixing ratio as  $q_l := q_c + q_p$  produces

$$\frac{dq_l}{dt} = (C_d + E_p) - \frac{1}{\rho} \nabla \cdot (\rho \mathbf{u}_\downarrow q_p) + D^{q_l} \quad (5)$$

that upon combining with (1c) leads to

$$\frac{1}{\theta} \frac{d\theta}{dt} - \frac{L}{c_p T} \frac{dq_l}{dt} = \frac{\mathcal{H}^*}{\theta} , \quad (6)$$

where  $\mathcal{H}^*$  subsumes all irreversible heat sink/sources in (1c) and (5). Assuming non-precipitating reversible processes and constant  $L/c_p T$ —justifiable for the special case of shallow convection governed by the incompressible Boussinesq equations [13]—(6) engenders two invariants  $\tilde{\theta} = \theta \exp[L q_l / c_p T]$  and  $q_t$ , a mere advection of which suffices to determine thermodynamic state of a displaced parcel in thermodynamic equilibrium with zero supersaturation [13]. This illustrates the essentially explicit nature of the invariant variables approach; cf. the penultimate paragraph of Introduction. Moreover, combining (4) and (1a) into the conservation form,

$$\frac{\partial \rho q_t}{\partial t} + \nabla \cdot (\rho \mathbf{u} q_t) = -\nabla \cdot (\rho \mathbf{u}_\downarrow q_p) + \nabla \cdot (\rho K_q \nabla q_t) , \quad (7)$$

shows that the system (1) conserves the total mass of water substance, subject to the boundary fluxes.<sup>3</sup> The first term on the rhs of (7) describes the precipitation fallout, with a velocity  $\mathbf{u}_\downarrow = (0, 0, -\vartheta)$  where the nonnegative terminal velocity  $\vartheta(\rho, q_p)$  follows a phenomenological power law; see (72) in

<sup>3</sup> A similar procedure could be applied to (6) leading to a compact entropy conservation principle under the stated simplifying assumptions.

Appendix A for an example. In principle, the sedimentation could be combined with the advection of precipitation on the lhs. However,  $\vartheta$  can reach values sufficiently large ( $\sim 10 \text{ m s}^{-1}$ ) to impair computational stability at vertical resolutions typical of cloud-resolving models. Consequently, it is retained as a forcing on the rhs, in anticipation of its bespoke time discretisation.

Setting  $q_t \equiv 0$  in (1b) recovers the familiar, advective form of the momentum equation for dry air [62].<sup>4</sup> This exposes the meaning of the coefficient in front of the pressure gradient in (1b) as the density potential temperature  $\theta_\rho$  normalised by a constant reference value  $\theta_0$ ; i.e.,

$$\frac{\theta(1 + q_v/\epsilon)}{\theta_0(1 + q_t)} = \frac{\theta_\rho}{\theta_0} := \Theta_\rho \quad (8)$$

This also reveals that, unlike in the dry case, the buoyancy term  $\mathbf{g}(1 - \theta_\rho/\theta_{\rho a})$  has been simplified in (1b) by truncating the Taylor series  $1/(1 + q_t) = 1 - q_t + \dots$  at  $q_t^2 \sim 10^{-4}$ —a verifiably useful approximation; cf. §5b in [3]. Similarly,

$$\theta' := \theta - \theta_a \quad \text{while} \quad q'_v = q_v - \frac{\theta}{\theta_a} q_{va} . \quad (9)$$

The second term on the rhs of (1c) combines latent heat sink/sources. In particular,  $L$  denotes the latent heat of condensation, whereas  $C_d$  and  $E_p$  symbolise, respectively, condensation rate of water vapour into cloud water and the growth/evaporation rate of precipitation due to diffusion of water vapour in supersaturated/subsaturated environment. These rates enter with the opposite sign the evolution equation of water vapour (1d), whereas  $C_d$  appears as a source on the rhs (1e), where  $A_p$  symbolises autoconversion of cloud water into precipitation (e.g., the initial source of rain) and  $C_p$  denotes growth of precipitation due to accretion of cloud condensate. The latter two terms enter with opposite sign the precipitation evolution on the rhs of (1f) accompanied by the precipitation growth/evaporation rate  $E_p$ . All these sink/source terms vanish in the absence of water substance, reducing (1d)-(1f) to “0 = 0” tautologies. Furthermore, except for the condensation rate  $C_d$ , all sink/source terms due to water substance phase changes are given by phenomenological formulae, expressed as power laws of the thermodynamic variables. For the purpose of this paper their precise form is unimportant, although they are all briefly listed in Appendix A for completeness; the reader interested in further details is referred to [13–17], and references therein. However the condensation-rate— $C_d$  forcing term on the rhs of (1c), (1d) and (1e)—is distinct. It is defined implicitly based on the assumptions that the water vapour is saturated in the presence of cloud water,

$$q_c > 0 \implies q_v = q_{vs} , \quad (10)$$

<sup>4</sup> Note,  $q_t \equiv 0 \implies q_v = q_c = q_p \equiv 0$ , due to the positivity of all water species.

and that the cloud water evaporates instantaneously in subsaturated conditions,

$$q_v < q_{vs} \implies q_c = 0, \quad (11)$$

where  $q_{vs}$  is the saturated mixing ratio of water vapour,

$$q_{vs} = \frac{\epsilon e_s}{p - e_s}, \quad (12)$$

with  $e_s$  denoting the saturated water vapour pressure,

$$e_s(T) = e_o \exp \left[ \frac{L}{R_v} \left( \frac{1}{T_o} - \frac{1}{T} \right) \right], \quad (13)$$

given  $T = \theta (p/p_o)^{R_d/c_p}$ ,  $p_o = 10^5$  Pa,  $e_o = 611$  Pa,  $T_o = 273.16$  K and  $L(T) \approx 2.53 \cdot 10^6$  J kg<sup>-1</sup>, which is an appropriate approximation for the warm-rain microphysics parameterisation assumed in this paper; cf. §2a in [14].

## 2.2 Conservative formulation

The conservative form of (1) actually solved in the FVM assumes a generalised curvilinear coordinate representation on a rotating sphere, upon which the corresponding PDEs can be compactly written as

$$\frac{\partial \mathcal{G}\rho}{\partial t} + \nabla \cdot (\mathcal{G}\rho \mathbf{v}) = 0, \quad (14a)$$

$$\begin{aligned} \frac{\partial \mathcal{G}\rho \mathbf{u}}{\partial t} + \nabla \cdot (\mathcal{G}\rho \mathbf{v} \otimes \mathbf{u}) = \mathcal{G}\rho \left( -\Theta_\rho \tilde{\mathbf{G}} \nabla \varphi \right. \\ \left. - \frac{\mathbf{g}}{\theta_a} (\theta' + \theta_a (\epsilon q'_v - q_c - q_p)) - \mathbf{f} \times \mathbf{u}' + \mathcal{M}' + \mathcal{D} \right), \end{aligned} \quad (14b)$$

$$\frac{\partial \mathcal{G}\rho \theta'}{\partial t} + \nabla \cdot (\mathcal{G}\rho \mathbf{v} \theta') = \mathcal{G}\rho \left( -\tilde{\mathbf{G}}^T \mathbf{u} \cdot \nabla \theta_a + \frac{L\theta}{c_p T} (C_d + E_p) + \mathcal{H} \right), \quad (14c)$$

$$\frac{\partial \mathcal{G}\rho q_{\dots}}{\partial t} + \nabla \cdot (\mathcal{G}\rho \mathbf{v} q_{\dots}) = \mathcal{G}\rho (\mathcal{R}^{q_{\dots}}). \quad (14d)$$

The PDEs (14) intertwine three distinct aspects of mathematical symbolism. First, (14d) consolidates (1d)-(1f), so  $q_{\dots}$  stands for  $q_v$ ,  $q_c$ , or  $q_p$  while  $\mathcal{R}^{q_{\dots}}$  marks their corresponding rhs forcings. Second, the focus on global applications extends (1b) with: i) the Coriolis acceleration  $\mathbf{f} \times \mathbf{u}'$  where  $\mathbf{f} \equiv 2\boldsymbol{\Omega}$  and  $\boldsymbol{\Omega}$  denotes a constant angular velocity of the rotating sphere; and ii) the metric forcings in the spherical domain

$$\mathcal{M}'(\mathbf{u}, \mathbf{u}_a, \theta_\rho / \theta_{\rho a}) = \mathcal{M}(\mathbf{u}) - (\theta_\rho / \theta_{\rho a}) \mathcal{M}(\mathbf{u}_a) \quad (15)$$

(cf. Appendix B). These extensions utilise a class of geostrophically balanced ambient flows

$$0 = -c_p \theta_{\rho a} \widetilde{\mathbf{G}} \nabla \pi_a - \mathbf{g} - \mathbf{f} \times \mathbf{u}_a + \mathcal{M}(\mathbf{u}_a) , \quad (16)$$

together with identically satisfied ambient mass continuity and entropy equations. Consequently,  $\mathbf{u}' = \mathbf{u} - (\theta_\rho / \theta_{\rho a}) \mathbf{u}_a$ . Third,  $(\mathbf{x}, t)$  refers to the coordinates of the generalised time-dependent frame, and  $\mathcal{G}(\mathbf{x}, t)$  denotes the Jacobian—so,  $\mathcal{G}^2$  is the determinant of the metric tensor that defines the fundamental metric in a space of interest where the problem is solved [37]. Following [56], for the remainder of the paper the nabla symbol  $\nabla$  refers to the vector of partial spatial derivatives in a computational space, whereby the physical meaning of the vector differential operators of gradient, curl and divergence is retrieved by combining nablas with metric coefficients, Jacobians, and relations between the various forms of velocities [37,53]. Consequently,  $\nabla \cdot (\dots)$  denotes the scalar product of spatial partial derivatives with a vector, so the total derivative underlying conservation form (14),  $d/dt = \partial/\partial t + \mathbf{v} \cdot \nabla$ , takes the velocity  $\mathbf{v} = \dot{\mathbf{x}}$  not necessarily equal to the physical velocity  $\mathbf{u}$  for which equations are solved. The  $\widetilde{\mathbf{G}} \nabla \varphi$  in the momentum equation symbolises the product of a known matrix of metric coefficients and the vector of partial derivatives, whereas  $\widetilde{\mathbf{G}}^T \mathbf{u} = \mathbf{v} - \mathbf{v}^g$  on the rhs of the entropy equation accounts for the mesh velocity  $\mathbf{v}^g$ , set to zero in the remainder of this paper. For the readers convenience, various metric coefficients are exemplified for the spherical frame in Appendix B.

Analogously to (1), the system (14) is supplied with the corresponding generalisation of (3), the advective form of the gas law (2), written compactly as

$$\frac{\partial \mathcal{G} \rho \varphi}{\partial t} + \nabla \cdot (\mathcal{G} \rho \mathbf{v} \varphi) = \mathcal{G} \rho \mathcal{R}^\varphi , \quad (17)$$

given the rhs forcing

$$\mathcal{R}^\varphi = -\xi \phi \frac{1}{\mathcal{G}} \nabla \cdot (\mathcal{G} \mathbf{v}) - \frac{1}{\mathcal{G} \rho} \nabla \cdot (\mathcal{G} \rho \mathbf{v} \phi_a) + \phi_a \frac{1}{\mathcal{G} \rho} \nabla \cdot (\mathcal{G} \rho \mathbf{v}) + \xi \phi \Pi , \quad (18)$$

where  $\Pi$  represents heat and mass sources/sinks from (1c) and (1d) aggregated on the rhs of (3)

$$\Pi \equiv \left( \frac{\mathcal{R}^\theta}{\theta} + \frac{\mathcal{R}^{q_v} / \epsilon}{1 + q_v / \epsilon} \right) . \quad (19)$$

The PDE (17) extends the equation (56) in [61] to account for the thermodynamic forcings according to the derivation detailed in the appendix A of [31].

### 3 NUMERICAL APPROXIMATIONS: PARCEL MODEL (**PCM**)

#### 3.1 Principal algorithm

To facilitate the presentation of a complete semi-implicit integrator for the generalised PDEs (14), it is constructive to consider first an isolated immiscible parcel in mechanical equilibrium with a prescribed steady environment. Equations governing such an elementary model are (1d)-(1f) with all  $D^{q\dots} \equiv 0$ , and the full  $\theta$  version of (1c) with  $\mathcal{H} \equiv 0$ ,

$$\frac{d\theta}{dt} = \frac{L\theta}{c_p T} (C_d + E_p) . \quad (20)$$

These equations can be compactly written as

$$\frac{d\Phi}{dt} = \mathbf{R} \equiv \mathbf{R}_c + \mathbf{R}_p , \quad (21)$$

with the vectors of variables and corresponding rhs forcing defined, respectively, as

$$\Phi = \begin{bmatrix} \theta \\ q_v \\ q_c \\ q_p \end{bmatrix} ; \quad \mathbf{R}_c = \begin{bmatrix} \frac{L\theta}{c_p T} C_d \\ -C_d \\ C_d \\ 0 \end{bmatrix} ; \quad \mathbf{R}_p = \begin{bmatrix} \frac{L\theta}{c_p T} E_p \\ -E_p \\ -A_p - C_p \\ A_p + C_p + E_p + F_p \end{bmatrix} , \quad (22)$$

where the shorthand for the fallout

$$F_p := -\frac{1}{\rho} \nabla \cdot (\rho \mathbf{u}_\downarrow q_p) \quad (23)$$

simplifies the notation. Recalling the discussion in Introduction,  $\mathbf{R}_c$  can be identified with rapid processes of cloud droplets condensation/evaporation, while  $\mathbf{R}_p$  with slow processes associated with precipitation formation, growth/evaporation and fallout. The algorithm for integrating (21) follows the all-scale approach of [17] inspired by the integral form of (21)

$$\Phi(\mathbf{x}, t) = \Phi(\mathbf{x}_o, t_o) + \int_{\mathcal{T}} (\mathbf{R}_c + \mathbf{R}_p) d\tau \quad (24)$$

that expresses the solution in an arbitrary point  $(\mathbf{x}, t)$  in terms of the solution at the foot  $(\mathbf{x}_o(\mathbf{x}, t), t_o)$  of the trajectory  $\mathcal{T}$ , connecting  $(\mathbf{x}_o, t_o)$  with  $(\mathbf{x}, t)$ , and the corresponding path integral of the rhs forcings. The discretisation of the integral in (24)

$$\Phi^{n+1} = \left( \Phi + 0.5\delta t \mathbf{R}_c \right)_o + 0.5\delta t \mathbf{R}_c^{n+1} + \delta t \langle \mathbf{R}_p \rangle_n^{n+1} \quad (25)$$

assumes the implicit trapezoidal rule and an explicit substepping, respectively, for the fast and slow forcings. Here discrete time levels  $t^n$  and  $t^{n+1} = t^n + \delta t$  correspond to  $t_o$  and  $t$  in (24), subscript  $o$  refers to the value at the foot of the trajectory,<sup>5</sup> and  $\langle \dots \rangle_n^{n+1}$  symbolises the mean value of the path integral evaluated over multiple substeps  $\delta\tau$ , such that  $\sum \delta\tau = \delta t$ .

### 3.2 Precipitation evaluation

The motivation behind (25) is a trade-off between the stability, accuracy and complexity of the time integration—justified by the disparities of the characteristic time scales associated with  $\mathcal{R}_c$  and  $\mathcal{R}_p$  as well as relative physical fidelity of the forcings, substantially lower for  $\mathcal{R}_p$  [14,17]. In particular, the substepping is important in coarsely resolved simulations of global flows, where the time step required for resolving precipitation may impose severe restrictions on the time step admitted for the dynamics [17]. Our lofty goal are global cloud-resolving simulations, where typically the mean value  $\langle \dots \rangle_n^{n+1}$  can be represented with explicit estimates of  $\mathcal{R}_p$  at  $t^{n+1}$  based on the past values of thermodynamic variables. The latter simplifies the presentation of the parcel algorithm, and facilitates concise incorporation of the substepping later.

The template algorithm (25) can have several alternative implementations with different overall accuracy and complexity levels. Here we describe a particular version—formally second-order accurate in the absence of precipitation, but first-order accurate otherwise—proven in research of all-scale moist atmospheric dynamics [30–32]. A single time step of (25) from  $t^n$  to  $t^{n+1}$  assumes that the advection procedure along the flow trajectory, "o", preserves the sign of transported fields. Given already available  $\Phi_o$  and  $\mathcal{R}_{co}$  at the foot, preliminary  $\mathcal{O}(\delta t)$  estimates of  $(A_p + C_p)^{n+1} = -\mathcal{R}_p^{qc}|^{n+1}$  and  $E_p^{n+1} = -\mathcal{R}_p^{qv}|^{n+1}$  are evaluated employing advected values of the thermodynamic variables in (73)-(75). This provides the estimate of  $q_p^{n+1}$  as

$$\tilde{q}_p^{n+1} = (q_p + \delta t \mathcal{R}^{qv})_o - \delta t (\widetilde{\mathcal{R}}_p^{qc} + \widetilde{\mathcal{R}}_p^{qv})^{n+1}. \quad (26)$$

Here  $\tilde{q}_p^{n+1}$  is merely an  $\mathcal{O}(\delta t)$  estimate of  $q_p^{n+1}$  solution, due to the lack of the fallout estimate on the rhs; whereas  $\mathcal{R}^{qv}|^n \equiv 0$  in the context of (25) is retained to acknowledge eventual contributions unaccounted for in the ideal parcel model—e.g. (54b) in Section 4.2 also accounts for diffusion. Moreover, the meaning of tildes over the forcings is special. Because the advection is sign preserving, the only non-physical loss of field positivity can come from inaccuracies in estimating the forcings. Thus, the estimated forcings are limited

<sup>5</sup> Consequently, the subscript "o" symbolises the field advected over  $\delta t$  [50,6].

according to

$$(q_c + \delta t \mathcal{R}^{q_c})_o + \delta t \mathcal{R}_p^{q_c}|^{n+1} \geq 0 \implies -\widetilde{\mathcal{R}}_p^{q_c}|^{n+1} = \min \left( -\mathcal{R}_p^{q_c}|^{n+1}, (\delta t^{-1} q_c + \mathcal{R}^{q_c})_o \right), \quad (27a)$$

$$(q_p + \delta t \mathcal{R}^{q_p})_o - \delta t (\widetilde{\mathcal{R}}_p^{q_c}|^{n+1} + \mathcal{R}_p^{q_v}|^{n+1}) \geq 0 \implies -\widetilde{\mathcal{R}}_p^{q_v}|^{n+1} = \max \left( \mathcal{R}_p^{q_v}|^{n+1}, -(\delta t^{-1} q_p + \mathcal{R}^{q_p})_o + \widetilde{\mathcal{R}}_p^{q_c}|^{n+1} \right), \quad (27b)$$

from which (27a) assures the precipitation autoconversion and accretion (the only sink of  $q_c$  due to  $q_p$ ) depleting no more  $q_c$  than estimated based on the past state, whereas (27b) ensures that subsequent precipitation evaporation depletes no more  $q_p$  than available  $\widetilde{q}_p^{n+1}$ .

The derived estimations of  $q_p$  and  $\mathcal{R}_p^{q_p}$  at  $t^{n+1}$  are still incomplete, as they do not account for the precipitation fallout  $F_p$ . However, the latter is a straightforward procedure that relies on an expedient use of a flux-form advection operator,

$$\mathcal{L}(\psi, \mathbf{v}, \rho^*, \delta\tau) := \psi - \frac{\delta\tau}{\rho^*} \nabla \cdot (\rho^* \mathbf{v} \psi), \quad (28)$$

the discrete implementation of which can assume a variety of suitable 1D advection schemes. In FVM, we employ either the implicit first-order-accurate upwind (alias donor-cell) scheme or a second-order-accurate MPDATA [55].<sup>6</sup> Having defined the  $\mathcal{L}$  operator in (28) the completion of  $q_p$  and  $\mathcal{R}_p^{q_p}$  estimates at  $t^{n+1}$  can be compactly written as

$$\widetilde{q}_p = \mathcal{L}(\widetilde{q}_p^{n+1}, \widetilde{\mathbf{G}}^T \mathbf{u}^\downarrow|^{n+1}, (\mathcal{G}\rho)^{n+1}, \delta t) \quad (29a)$$

$$\widetilde{\mathcal{R}}_p^{q_p}|^{n+1} = -(\widetilde{\mathcal{R}}_p^{q_c} + \widetilde{\mathcal{R}}_p^{q_v})^{n+1} + (\widetilde{q}_p - \widetilde{q}_p^{n+1})/\delta t, \quad (29b)$$

where  $\mathbf{u}^\downarrow|^{n+1}$  depends on the current estimates of its arguments in (72).

In cloud-resolving simulations, where the time scales of resolved dynamics and precipitation evolution are comparable, (29) completes the evaluation of explicit estimates of precipitation mixing ratio and, in fact, of all components of slow forcings  $\langle \mathcal{R}_p \rangle_n^{n+1}$  in (25). This is evident when writing a complete set of available estimates of thermodynamic fields evolved due to action of slow forcings:

$$\widetilde{\theta}^{n+1} = (\theta + \delta t \mathcal{R}^\theta)_o - \delta t \Lambda^* \widetilde{\mathcal{R}}_p^{q_v}|^{n+1}, \quad (30a)$$

$$\widetilde{q}_v^{n+1} = (q_v + \delta t \mathcal{R}^{q_v})_o + \delta t \widetilde{\mathcal{R}}_p^{q_v}|^{n+1}, \quad (30b)$$

<sup>6</sup> The implicit donor-cell is particularly convenient due it is unconditional stability, sign preservation and simplicity owing to the precipitation downward movement.

$$\widetilde{q}_c^{n+1} = (q_c + \delta t \mathcal{R}^{q_c})_o + \delta t \widetilde{\mathcal{R}}_p^{q_c} |^{n+1}, \quad (30c)$$

$$\widetilde{q}_p^{n+1} = (q_p + \delta t \mathcal{R}^{q_p})_o + \delta t \widetilde{\mathcal{R}}_p^{q_p} |^{n+1}; \quad (30d)$$

where the abbreviated notation,

$$\Lambda^* := \frac{L}{c_p} \left( \frac{\widetilde{\theta}}{T} \right)^{n+1} \implies \Lambda^* = \frac{L}{c_p} \widetilde{(\pi)}^{n+1}, \quad (31)$$

has been introduced in (30a) to streamline further presentation, and the approximation of the  $\widetilde{(\theta/T)}^{n+1}$  ratio, temporarily assumed to be known, is yet to be discussed.

Notably, in cloud-resolving simulations only the  $\widetilde{\mathcal{R}}_p^{q_\dots}$  forcings are required, while there is no further use for the  $\widetilde{(\cdot)}^{n+1}$  fields' estimates, unless higher order variants of the parcel scheme are desired. However in coarse large scale simulations, (30) summarises the contents of a single substep  $\delta\tau$  that is to be repeated as described above, until  $\sum \delta\tau = \delta t$ , to re-evaluate  $\vartheta$ ,  $A_p$ ,  $C_p$  and  $E_p$ —exemplified in Appendix A—while evaluating and summing all components of  $\langle \mathcal{R}_p \rangle_n^{n+1}$ , such that

$$\delta t \langle \mathcal{R}_p \rangle_n^{n+1} = \sum_{\nu=0}^{\mathcal{N}} \delta\tau^\nu \widetilde{\mathcal{R}}_p^\nu = \sum_{\nu=0}^{\mathcal{N}} \delta\tau^\nu \begin{bmatrix} -\Lambda^* \widetilde{\mathcal{R}}_p^{q_v} \\ \widetilde{\mathcal{R}}_p^{q_v} \\ \widetilde{\mathcal{R}}_p^{q_c} \\ \widetilde{\mathcal{R}}_p^{q_p} \end{bmatrix}^\nu, \quad (32a)$$

$$\widetilde{\mathcal{R}}_p^{\nu=0} = \widetilde{\mathcal{R}}_p^n \equiv 0, \quad \widetilde{\mathcal{R}}_p^{\nu=\mathcal{N}} = \widetilde{\mathcal{R}}_p^{n+1}, \quad \sum_{\nu=0}^{\mathcal{N}} \delta\tau^\nu = \delta t. \quad (32b)$$

Having accomplished the calculation of slow forcings, we turn the attention back to (25).

In preparation for completing (25) we note that limiting of forcings in (27) ensured positivity of water species in (30)—particularly important for the substepped model—but not necessarily in (25). To assure the species positivity in (25), while conserving the water substance and energy, the cumulative  $\delta t \langle \mathcal{R}_p \rangle_n^{n+1}$  forcings are limited as follows:

$$(q_c + 0.5\delta t \mathcal{R}^{q_c})_o + \delta t \langle \mathcal{R}_p^{q_c} \rangle_n^{n+1} \geq 0 \implies \widetilde{\langle \mathcal{R}_p^{q_c} \rangle}^{n+1} = \max \left( \langle \mathcal{R}_p^{q_c} \rangle_n^{n+1}, -\delta t^{-1} (q_c + 0.5\delta t \mathcal{R}^{q_c})_o \right), \quad (33a)$$

$$(q_p + 0.5\delta t \mathcal{R}^{q_p})_o + \delta t \langle \mathcal{R}_p^{q_p} \rangle_n^{n+1} \geq 0 \implies \widetilde{\langle \mathcal{R}_p^{q_p} \rangle}^{n+1} = \max \left( \langle \mathcal{R}_p^{q_p} \rangle_n^{n+1}, -\delta t^{-1} (q_p + 0.5\delta t \mathcal{R}^{q_p})_o \right), \quad (33b)$$

$$\Delta_{q_l} = \langle \widetilde{\mathcal{R}}_p^{q_c} \rangle^{n+1} - \langle \mathcal{R}_p^{q_c} \rangle^{n+1} + \langle \widetilde{\mathcal{R}}_p^{q_p} \rangle^{n+1} - \langle \mathcal{R}_p^{q_p} \rangle^{n+1} \implies \quad (33c)$$

$$\langle \widetilde{\mathcal{R}}_p^{q_v} \rangle^{n+1} = \langle \mathcal{R}_p^{q_v} \rangle_n^{n+1} - \Delta_{q_l} ,$$

$$\langle \widetilde{\mathcal{R}}_p^\theta \rangle^{n+1} = \langle \mathcal{R}_p^\theta \rangle^{n+1} + \Lambda^* \Delta_{q_l} \quad (33d)$$

Subsequently, the complete explicit part of the solution (25) is created as

$$\widehat{\Phi} := \left( \Phi + 0.5\delta t \mathcal{R}_c \right)_o + \delta t \langle \widetilde{\mathcal{R}}_p \rangle_n^{n+1} , \quad (34)$$

with components of  $\langle \widetilde{\mathcal{R}}_p \rangle_n^{n+1}$  specified in (33). This reduces (25) to

$$\Phi^{n+1} = \widehat{\Phi} + 0.5\delta t \mathcal{R}_c^{n+1} , \quad (35)$$

an implicit problem for  $\Phi^{n+1}$  discussed next.

### 3.3 Condensation/evaporation of cloud water

The significance of (35) is constraining the thermodynamic variables to assure thermodynamic equilibrium (10)-(13) of the evolved parcel. Technically, this requires determining the increment of cloud water mixing ratio  $\Delta q_c = 0.5\delta t C_d$ , either via condensation ( $\Delta q_c > 0$ ) or evaporation ( $\Delta q_c < 0$ ), such that the solution of (35) satisfies:

$$q_v^{n+1} = \widehat{q}_v - \Delta q_c = q_{vs} \left( \widehat{\theta} + \Lambda^* \Delta q_c, \Lambda^* \right) , \quad \text{if } (\widehat{q}_c + \Delta q_c) > 0 ; \quad (36a)$$

$$q_c^{n+1} = \widehat{q}_c + \Delta q_c = 0 , \quad \text{if } (\widehat{q}_v - \Delta q_c) < q_{vs} \left( \widehat{\theta} + \Lambda^* \Delta q_c, \Lambda^* \right) . \quad (36b)$$

Because of the functional form of  $q_{vs}$  in (12), (36) together with the usual positivity constraints forms the system of implicit transcendental inequalities, the solution of which commences with unfolding the saturation condition in (36a). The latter implies

$$\Delta q_c = \widehat{q}_v - q_{vs} \left( \widehat{\theta} + \Lambda^* \Delta q_c, \Lambda^* \right) \approx \widehat{q}_v - q_{vs}(\widehat{\theta}, \Lambda^*) - \left. \frac{dq_{vs}}{d\Delta q_c} \right|_{\Delta q_c=0} \Delta q_c , \quad (37)$$

where the first-order Taylor series approximation is justified, as typically  $\Lambda^* |\Delta q_c| \ll \widehat{\theta}$ . The linearised solution implied by (37) can be explicitly written as

$$\Delta q_c = \left[ \widehat{q}_v - q_{vs} \left( \widehat{\theta}, \Lambda^* \right) \right] \left[ 1 + \left. \frac{dq_{vs}}{d\Delta q_c} \right|_{\Delta q_c=0} \right]^{-1} , \quad (38a)$$

$$\left. \frac{dq_{vs}}{d\Delta q_c} \right|_{\Delta q_c=0} = q_{vs} \left( \widehat{\theta}, \Lambda^* \right) \left[ 1 - e_s(\widehat{\theta}, \Lambda^*)/p^* \right]^{-1} \frac{c_p}{R_v} \left( \frac{\Lambda^*}{\widehat{\theta}} \right)^2 , \quad (38b)$$

$$e_s(\widehat{\theta}, \Lambda^*) \equiv e_s(\widehat{T}) \quad \text{at} \quad \widehat{T} = \frac{L}{c_p} \frac{\widehat{\theta}}{\Lambda^*}, \quad \text{and} \quad p^* = p_0 \left( \frac{c_p}{L} \Lambda^* \right)^{R_d/c_p}. \quad (38c)$$

Standardly, we supplement the linearised solution (38) with one Newton-Raphson iteration

$$\widehat{\theta}^+ = \widehat{\theta} + \Lambda^* \Delta q_c, \quad \widehat{q}_v^+ = \widehat{q}_v - \Delta q_c \quad (39a)$$

$$\Delta^+ q_c = \Delta q_c + \text{EQS}_{(38)} \left( \widehat{q}_v^+, \widehat{\theta}^+ \right). \quad (39b)$$

which improves on the linearised result in problems with large  $\delta t$  and coarse resolutions [13]; optionally, (39) can be further repeated if required.

Upon completing (39), final  $\Delta^+ q_c$  is limited according to

$$\widetilde{\Delta^+ q_c} = \min[\widehat{q}_v, \max(-\widehat{q}_c, \Delta^+ q_c)] \quad (40)$$

that ensures positivity of final solutions for water vapour and cloud water mixing ratios in

$$q_v^{n+1} = \widetilde{\widehat{q}_v} - \widetilde{\Delta^+ q_c} \quad (41a)$$

$$q_c^{n+1} = \widehat{q}_c + \widetilde{\Delta^+ q_c} \quad (41b)$$

$$\theta^{n+1} = \widehat{\theta} + \Lambda^* \widetilde{\Delta^+ q_c} \quad (41c)$$

Furthermore, to assure positivity of the future initial fields, assumed in the second paragraph of Section 3.2 for the subsequent time step, the limiting of the condensation rate (40) is repeated with respect to the updated fields (41),

$$\widetilde{\widetilde{\Delta^+ q_c}} = \min[q_v^{n+1}, \max(-q_c^{n+1}, \widetilde{\Delta^+ q_c})], \quad (42)$$

upon which specification of the rhs forcings  $\mathbf{R} = \mathbf{R}_c$  in (21) for the subsequent time step initial condition

$$\mathcal{R}^{q_v}|^{n+1} = -(0.5\delta t)^{-1} \widetilde{\widetilde{\Delta^+ q_c}} \quad (43a)$$

$$\mathcal{R}^{q_c}|^{n+1} = -\mathcal{R}^{q_v}|^{n+1} \quad (43b)$$

$$\mathcal{R}^\theta|^{n+1} = \Lambda^* \mathcal{R}^{q_c}|^{n+1} \quad (43c)$$

completes the discrete approximation (25) of the formal integral (24) of (21)—given the availability of  $\Lambda^*$ , defined in (31). Formally,  $\Lambda^*$  depends on the  $n + 1$  value of the Exner pressure, which is however unavailable until the very end of the full time-step advancement of the entire dynamical model, concluded by the solution of the elliptic pressure equation. A viable option is to employ in (31) a pressure estimate based on the past fields' values. An even simpler option is the physically motivated approximation

$$\pi^{-1} = \frac{\theta}{T} \approx \frac{\theta_a}{T_a} = \pi_a^{-1}, \quad (44)$$

verified for needs of bulk parametrisations of cloud microphysics in atmospheric models across scales [30–32].

### 3.4 Extensions

Because of its relative physical simplicity, the warm-rain bulk microphysics parametrisation is attractive, and de facto standard [8], as a first step for incorporating moist processes in nonhydrostatic atmospheric flow solvers. Albeit important per se, the warm-rain parametrisation does not account for a broad range of equally important processes, the most apparent of which are those associated with the solid phase of the water substance. The accommodation of the solid phase can, again, vary widely in physical complexity [68]. For instance, a “simple ice” parametrisation [15] extends the classical warm-rain approach to admit both liquid and solid phase within the mixing ratios of cloud condensate  $q_c$  and precipitation  $q_p$  depending upon the local temperature; and such a simple approach is already available in FVM as an option. More complex parametrisations account for various ice forms such as cloud ice, snow, hail, and graupel. Each of such species is subject to its own phenomenological laws of evolution. Furthermore, such parametrisations can branch further into single- and double-moment schemes, with the former predicting only mixing ratios of cloud and precipitation species, whereas the latter also accounting for variable particle size distributions; e.g. [19] versus [21]. Altogether, this adds substantial physical complexity to the warm-rain parametrisation. While cloud and precipitation microphysics is a large and active research area, and the quest for an optimal parametrisation continues [12,19], the single-moment multi-species microphysics is nowadays standard in global weather prediction [11].

In the context of the considerations above, it is important to comment on the broader applicability of the documented  $\mathcal{PCM}$  scheme. In essence, the scheme relies on the assumption of universally preserved positivity of physically nonnegative fields and, to a lesser extent, on the separation of microphysical processes into slow and fast, respectively, for precipitation evolution and condensation/evaporation of cloud water. From the perspective of numerics, the latter one is rather helpful than essential, as one can always split integrals of the rhs forcings into, e.g. left/right Riemann sums or trapezoidal rules based on the accuracy arguments. On the other hand, given a sign-preserving advection, the positivity arguments provide solid foundation for clipping truncation errors in the rhs forcings to assure physical realisability of complete solutions. The same approach thus applies to multi-species schemes, with an obvious consequence of advecting more fields and solving larger systems of inequalities. Furthermore, the implicit procedure for evaluating the condensation rate, §3.3, can be extended to account for finite supersaturations [20].

## 4 NUMERICAL APPROXIMATIONS: MOIST-PRECIPIATING DYNAMICS

### 4.1 Non-oscillatory forward-in-time template

The equations comprising system (14) can be written in a compact form of the generalised transport equation for an arbitrary scalar variable  $\Psi$ ,

$$\frac{\partial G\Psi}{\partial t} + \nabla \cdot (\mathbf{V}\Psi) = G\mathcal{R} , \quad (45)$$

in which the vector field  $\mathbf{V}$  as well as scalar fields  $G$  and  $\mathcal{R}$  are assumed to be known functions of time and space. For the mass continuity equation  $\mathcal{R} \equiv 0$ ,  $\Psi \equiv \rho$ ,  $G \equiv \mathcal{G}$ , so  $\mathbf{V} = \mathcal{G}\mathbf{v}$ . For all other equations,  $\Psi$  represents the specific variables—expressing in (14) fluid properties in a unit of mass—namely, components of the physical velocity vector  $\mathbf{u}$ , the potential temperature  $\theta$  together with its perturbations  $\theta'$ , and mixing ratios  $q_{\dots}$ ; whereas the density  $\rho$  is absorbed in  $G \equiv \mathcal{G}\rho$ . Then  $\mathcal{R}$  represents the corresponding parenthetic terms on the rhs in (14), and  $\mathbf{V} \equiv G\mathbf{v} = \mathcal{G}\rho\mathbf{v}$  amounts to the mass flux in (14a). Formulating numerical integrators of (14) according to the procedures adopted for (45) assures the compatibility of conservative advection of all specific variables with the mass continuity [61,62].

A key building block for semi-implicit integrators of the PDE system (14) is a non-oscillatory forward-in-time (NFT)<sup>7</sup> template algorithm for (45)

$$\Psi_{\mathbf{i}}^{n+1} = \mathcal{A}_{\mathbf{i}} \left( \tilde{\Psi}^n, \mathbf{V}^{n+1/2}, G^n, G^{n+1} \right) + 0.5\delta t \mathcal{R}_{\mathbf{i}}^{n+1} , \quad \tilde{\Psi}^n \equiv \Psi^n + 0.5\delta t \mathcal{R}^n . \quad (46)$$

Here,  $\mathcal{A}$  is a shorthand for the NFT advection transport operator MPDATA (for multidimensional positive definite advection transport algorithm) [55,62,29]. Furthermore, the index  $\mathbf{i}$  symbolises position on the computational grid, and the advector  $\mathbf{V}^{n+1/2}$  is an  $\mathcal{O}(\delta t^2)$  estimate of  $\mathbf{V}$  at the intermediate time level. The template (46) is congruent with the trapezoidal-rule trajectory integral of the ODE underlying (45) [51,57], as illustrated by (25) in the absence of precipitation. Its respective Euler-forward,

$$\Psi_{\mathbf{i}}^{n+1} = \mathcal{A}_{\mathbf{i}} \left( \Psi^n + \delta t \mathcal{R}^n, \mathbf{V}^{n+1/2}, G^n, G^{n+1} \right) , \quad (47)$$

and Euler-backward,

$$\Psi_{\mathbf{i}}^{n+1} = \mathcal{A}_{\mathbf{i}} \left( \Psi^n, \mathbf{V}^{n+1/2}, G^n, G^{n+1} \right) + \delta t \mathcal{R}_{\mathbf{i}}^{n+1} , \quad (48)$$

<sup>7</sup> Inspired by [70], “non-oscillatory forward-in-time” labels a class of second-order-accurate algorithms built on two-time-level nonlinear advection techniques that suppress numerical oscillations characteristic of higher-order linear schemes.

forms as well as their combinations for selected counterparts of  $\mathcal{R}$  will be also employed in the subsequent discussions.

Notably, for any  $\mathcal{O}(\delta t^2)$  estimates of  $\mathcal{R}^n$  and  $\mathcal{R}^{n+1}$  on the rhs of (46), the solution  $\Psi_{\mathbf{i}}^{n+1}$  is second-order-accurate, given  $\mathcal{A}$  assures the second-order-accurate homogeneous transport [51]; see also [61] for a recent comprehensive discussion. On the other hand, the trapezoidal-rule template (46) can be also used to describe mixed integrals with respect to rhs forcings, by judiciously manipulating forcings' definitions at the template input. For example, conservative form of (25) can be written in the formalism of (46) as

$$\Phi_{\mathbf{i}}^{n+1} = \mathcal{A}_{\mathbf{i}} \left( \tilde{\Phi}^n, \mathbf{V}^{n+1/2}, G^n, G^{n+1} \right) + 0.5\delta t \mathcal{R}_{\mathbf{i}}^{n+1}, \quad \tilde{\Phi}^n \equiv \Phi^n + 0.5\delta t \mathcal{R}^n, \quad (49)$$

given

$$\mathcal{R}^n = \mathcal{R}_c^n, \quad \mathcal{R}^{n+1} = \mathcal{R}_c^{n+1} + 2\langle \mathcal{R}_p \rangle_n^{n+1}. \quad (50)$$

A virtue of such a notation is that it enables a concise description of complex semi-implicit integrators discussed next—see (57a) for an example—while at the same time reflecting the actual structure of the model code; cf. section 3.1 in [59] for complementary discussion.

#### 4.2 Semi-implicit integrators

In the system (14), only the mass continuity equation (14a) is homogeneous, whereas all remaining equations generally have non-vanishing right-hand-sides that depend on the prognosed model variables. In consequence, the entire model algorithm can be reduced to three conceptually distinct stages.

The first stage solves (14a) while taking the advantage of it to explicitly provide the advectors that enter the first term on the rhs of (46) in transport of the specific variables. Namely, the provisional advector  $\mathbf{V}^{n+1/2} = (\mathcal{G}\mathbf{v})^{n+1/2}$ , evaluated by linear extrapolation from  $t^{n-1}$  and  $t^n$  at faces of computational cells (cf. Section 4.4), is used in the density advection,

$$\rho_{\mathbf{i}}^{n+1} = \mathcal{A}_{\mathbf{i}} \left( \rho^n, (\mathcal{G}\mathbf{v})^{n+1/2}, \mathcal{G}^n, \mathcal{G}^{n+1} \right) \implies \mathbf{V}^{n+1/2} = \overline{(\mathcal{G}\rho\mathbf{v})}^{n+1/2}, \quad (51)$$

while updating the density, and concomitantly evaluating the advectors for transport of  $\mathbf{u}$ ,  $\theta'$ ,  $\theta$  and  $q_{\dots}$  in (14) as cumulative directional mass fluxes; see [61] for an exposition and [62] for details of the implementation in FVM.

The second stage evaluates the explicit components required in the semi-implicit integrals of the momentum, entropy, and water-substance mixing-ratio equations in (14). This stage involves a few distinct steps. First, the explicit

transport components of the (46) template are evaluated for specific momenta and entropy perturbations as

$$\widehat{\mathbf{u}}_{\mathbf{i}} = \mathcal{A}_{\mathbf{i}} \left( \widetilde{\mathbf{u}}, \mathbf{V}^{n+1/2}, \rho^{*n}, \rho^{*n+1} \right), \quad (52a)$$

$$\widehat{\theta}'_{\mathbf{i}} = \mathcal{A}_{\mathbf{i}} \left( \widetilde{\theta}', \mathbf{V}^{n+1/2}, \rho^{*n}, \rho^{*n+1} \right), \quad (52b)$$

where  $\widetilde{\mathbf{u}}$  and  $\widetilde{\theta}'$  account for complete forcings on the rhs of (1b) and (1c), respectively, and the effective densities,  $\rho^* := \mathcal{G}\rho$ , are specified as  $\rho^{*n} = \mathcal{G}^n \rho^n$  and  $\rho^{*n+1} = \mathcal{G}^{n+1} \rho^{n+1}$ .

Second, a distinct block in the similar spirit follows for the moist specific variables discussed in Section 3

$$\widehat{\theta}_{\mathbf{i}} = \mathcal{A}_{\mathbf{i}} \left( \widetilde{\theta}, \mathbf{V}^{n+1/2}, \rho^{*n}, \rho^{*n+1} \right), \quad \widetilde{\theta} = \theta^n + 0.5\delta t \left( \mathcal{R}^\theta + 2\mathcal{H} \right)^n \quad (53a)$$

$$\widehat{q}_{\dots\mathbf{i}} = \mathcal{A}_{\mathbf{i}} \left( \widetilde{q}_{\dots}, \mathbf{V}^{n+1/2}, \rho^{*n}, \rho^{*n+1} \right), \quad \widetilde{q}_{\dots} = q_{\dots}^n + 0.5\delta t \left( \mathcal{R}^{q_{\dots}} + 2D(q_{\dots}) \right)^n \quad (53b)$$

where  $\mathcal{R}^\theta$  and the  $\mathcal{R}^{q_{\dots}}$  were specified in (43) at the preceding time step. Bespoke to moist dynamics, (53) are also supplied with advected forcings

$$\widehat{\mathcal{R}}^\theta_{\mathbf{i}} = \mathcal{A}_{\mathbf{i}} \left( \mathcal{R}^\theta|_n + \mathcal{H}(q_{\dots})|_n, \mathbf{V}^{n+1/2}, \rho^{*n}, \rho^{*n+1} \right), \quad (54a)$$

$$\widehat{\mathcal{R}}^{q_{\dots}\mathbf{i}} = \mathcal{A}_{\mathbf{i}} \left( \mathcal{R}^{q_{\dots}}|_n + D(q_{\dots})|_n, \mathbf{V}^{n+1/2}, \rho^{*n}, \rho^{*n+1} \right), \quad (54b)$$

required within (25) for a complete first-order-accurate estimate of the future thermodynamic state in the precipitation evaluation (30) and then for completing the explicit part of the solution in (34).

Third, the “parcel model” of Section 3 completes the integrals of (14d) and (20)—now both with account for the dissipative processes via (53) and (54). This step can be symbolised as

$$\mathcal{PCM} \left( \widehat{\theta}, \widehat{q}_{\dots}, \widehat{\mathcal{R}}^\theta, \widehat{\mathcal{R}}^{q_{\dots}} \right) \implies \left[ \theta, q_{\dots}, \mathcal{R}^\theta, \mathcal{R}^{q_{\dots}} \right]^{n+1}, \quad (55)$$

which completes the second stage. Noteworthy, the  $\mathcal{PCM}$  procedure provides an updated total potential temperature  $\theta^{n+1}$  and, thus, the full  $\theta_\rho^{n+1}$ . These estimates could be used in the buoyancy term on the rhs of (14b) while evaluating the  $\mathcal{R}_{\mathbf{i}}^{n+1}$  forcing in the template algorithm (46). On one hand, this would eliminate the need for advancing the  $\theta'$  perturbation variable. On the other hand, this would result in an explicitly evaluated buoyancy term—in the spirit of Runge-Kutta schemes [50,51]—imposing severe limits on the model time step for global flows [61], where the phase velocity of internal gravity waves supported by vertical stratification can be comparable with the speed of sound (§1.2 in [24]). The latter is the primary reason for the incompatibility of explicitly evolved invariant variables and large-time-step semi-implicit schemes as mentioned in the introduction. Consequently,  $\theta'$  remains a primary

dependent model variable, whereas full  $\theta$  is an explicit estimate required for the  $\mathcal{PCM}$  and for a first guess in the coefficients on the rhs of (14b). After completing the solution at  $t^{n+1}$ , this full  $\theta$  is redefined using the updated  $\theta'$ ; so at the subsequent time step, starting from the current instant  $t^{n+1}$  relabelled to  $t^n$ ,  $\theta^n = (\theta' + \theta_a)^n$ .

The third stage culminates the entire solution procedure. It employs all the explicit elements developed so far, to complete semi-implicit integrals of the specific momentum and entropy perturbations. To account for nonlinearity of the rhs in (14b)—due to the dependence of the coefficients on  $\theta'$  in the pressure gradient, Coriolis and metric forces as well as the nonlinearity of the metric forces in terms of the velocity components—the template algorithm (46) is, generally, executed iteratively lagging nonlinear terms behind.<sup>8</sup> To simplify notation, the lagged terms will be denoted by the superscript  $\star$ , variables without superscripts will represent subsequent iterates of the solution future values at  $t^{n+1}$ , whereas variables marked with superscript  $n+1$  will refer to already-updated variables such as density and water substance mixing ratios at  $t^{n+1}$ . Consequently,

$$\theta'_i = \widehat{\theta}'_i - 0.5\delta t \left( \widetilde{\mathbf{G}}^T \mathbf{u} \cdot \nabla \theta_a \right)_i \quad (56a)$$

$$\begin{aligned} \mathbf{u}_i = \widehat{\mathbf{u}}_i - 0.5\delta t \left( \Theta_\rho^\star \widetilde{\mathbf{G}} \nabla \varphi + \frac{\mathbf{g}}{\theta_a} [\theta' + \mathcal{B}^{q,n+1}] \right)_i \\ - 0.5\delta t \left( \mathbf{f} \times \left[ \mathbf{u} - \frac{\theta_\rho^\star}{\theta_{\rho a}} \mathbf{u}_a \right] - \mathcal{M}' \left( \mathbf{u}^\star, \mathbf{u}_a, \frac{\theta_\rho^\star}{\theta_{\rho a}} \right) \right)_i ; \end{aligned} \quad (56b)$$

where

$$\widehat{\theta}' = \widehat{\theta}' + 0.5\delta t \left( \mathcal{R}^\theta + 2 \langle \widetilde{\mathcal{R}}_p^\theta \rangle \right)^{n+1}, \quad (57a)$$

$$\Theta_\rho^\star = \frac{\theta_\rho^\star}{\theta_0} = \frac{\theta^\star (1 + q_v^{n+1} / \epsilon)}{\theta_0 (1 + q_t^{n+1})}, \quad (57b)$$

while

$$\mathcal{B}^q := \theta_a (\varepsilon q'_v - q_c - q_p) \quad (58)$$

is a shorthand for moisture contributions to the density potential temperature perturbation in the buoyancy force; recall that the functional dependence of the  $\mathcal{M}'$  on its arguments has been specified in (15). Furthermore, resetting the full  $\theta$  directly follows the velocity update at the end of each iteration as

$$\theta_i = \left( \widehat{\theta}' - 0.5\delta t \widetilde{\mathbf{G}}^T \mathbf{u} \cdot \nabla \theta_a + \theta_a \right)_i, \quad (59)$$

<sup>8</sup> Typically, a few fixed-point iterations suffice for practically converged solution; see [57,59,61] for implementations in, respectively, gas dynamics, magnetohydrodynamics and generalised PDEs (14), all in the context of the FT template (46).

whereas its first guess can either use the  $\mathcal{PCM}$  estimate, or the Euler-forward estimate (47) generated as

$$\theta_{\mathbf{i}}^0 = \mathcal{A}_{\mathbf{i}} \left( \theta^n + \delta t (\mathcal{R}^\theta + \mathcal{H})^n, \mathbf{V}^{n+1/2}, \rho^{*n}, \rho^{*n+1} \right), \quad (60)$$

in analogy to the dry case [61,62]. As far as the velocity lagging in the metric forces is concerned, its first guess  $\mathbf{u}_{\mathbf{i}}^0$  is obtained by linear extrapolation from  $t^{n-1}$  and  $t^n$  to  $t^{n+1}$ . With this design, the inviscid non-precipitating solution is second-order-accurate even for a single iteration, and two iterations give already close approximation to the trapezoidal integral [57].

The scheme outlined in (56)-(59) contains implicit trapezoidal integrals of pressure gradient, buoyancy and Coriolis terms with the coefficients, dependent on the full potential temperature, and metric forces evaluated explicitly. The derivation of the closed-form expression for the velocity update is straightforward for the colocated data arrangement employed in the FVM [62]. Specifically, the future value of  $\theta'$  is substituted in the buoyancy term on the rhs of (56b) with the rhs of (56a), and all terms depending on the future value of  $\mathbf{u}$  are gathered on the lhs of the momentum scheme—while dropping the spatial grid index  $\mathbf{i}$  everywhere, as all dependent variables, coefficients and terms are colocated in (56)-(59). For the large-time-step compressible equations addressed here, this results in

$$\begin{aligned} \mathbf{u} + 0.5\delta t \mathbf{f} \times \mathbf{u} - (0.5\delta t)^2 \frac{\mathbf{g}}{\theta_a} \widetilde{\mathbf{G}}^T \mathbf{u} \cdot \nabla \theta_a = & \quad (61) \\ \widehat{\mathbf{u}} - 0.5\delta t \left( \frac{\mathbf{g}}{\theta_a} \left[ \widehat{\theta}' + \mathcal{B}^{q,n+1} \right] - \mathbf{f} \times \frac{\theta_\rho^*}{\theta_{\rho a}} \mathbf{u}_a - \mathcal{M}' \left( \mathbf{u}^*, \mathbf{u}_a, \frac{\theta_\rho^*}{\theta_{\rho a}} \right) \right) \\ - 0.5\delta t \Theta^* \widetilde{\mathbf{G}} \nabla \varphi \equiv & \widehat{\mathbf{u}} - 0.5\delta t \Theta_\rho^* \widetilde{\mathbf{G}} \nabla \varphi, \end{aligned}$$

which symbolises a system of three linear algebraic equations with three unknown components of the velocity vector  $\mathbf{u}$  at each point of the colocated grid. Viewing the lhs of (61) as a linear operator  $\mathbf{L}$  acting on the velocity vector  $\mathbf{u}$ ,

$$\mathbf{L} \mathbf{u} = \widehat{\mathbf{u}} - 0.5\delta t \Theta_\rho^* \widetilde{\mathbf{G}} \nabla \varphi, \quad (62)$$

the closed-form expression for the velocity update may be symbolised as

$$\mathbf{u} = \check{\mathbf{u}} - \mathbf{C} \nabla \varphi, \quad (63)$$

where  $\check{\mathbf{u}} = \mathbf{L}^{-1} \widehat{\mathbf{u}}$ , and  $\mathbf{C} = \mathbf{L}^{-1} 0.5 \delta t \Theta_\rho^* \widetilde{\mathbf{G}}$  denotes a  $3 \times 3$  matrix of known coefficients.<sup>9</sup> Noting that the potential temperature perturbation  $\theta'$  is updated according to (56a) upon the final velocity update, the only lacking element to

<sup>9</sup> The expanded forms of (63) in either tensorial or explicit component notation can be found in [37] and [58,60], respectively.

complete the solution at each iteration is the pressure perturbation  $\varphi$ . This brings the gas law back into focus, as discussed next.

### 4.3 Elliptic boundary value problem

In principle, the pressure perturbation can be evaluated straightforwardly from the gas law (2). This leads to a viable acoustic option of the solver, which resolves propagation of sound waves in the spirit of gas dynamics for all speed flows [57]. While impractical for NWP, such an option provides a useful reference for large-time-step simulations of low Mach number atmospheric flows [61,30–32]. Otherwise, a boundary value problem (BVPs) for  $\varphi$  supersedes (2) with its advective form (17) that, when integrated consistently with the model numerics, can ensure computational stability independent of the speed of sound [61,31,62]. In particular, recalling from Section 2.2 that in stationary coordinates  $\mathbf{v} = \widetilde{\mathbf{G}}^T \mathbf{u}$ , (63) entails

$$\mathbf{v} = \check{\mathbf{v}} - \widetilde{\mathbf{G}}^T \mathbf{C} \nabla \varphi . \quad (64)$$

Thereupon, manipulating the terms on the rhs of (17)—see [61,31] for details—leads to the PDE

$$\frac{\partial \mathcal{G} \rho \varphi}{\partial t} + \nabla \cdot (\mathcal{G} \rho \mathbf{v} \varphi) = \mathcal{G} \rho \sum_{\ell=1}^3 \left( \frac{a_\ell}{\zeta_\ell} \nabla \cdot \zeta_\ell (\check{\mathbf{v}} - \widetilde{\mathbf{G}}^T \mathbf{C} \nabla \varphi) \right) + b\varphi + c , \quad (65)$$

where coefficients  $a_\ell$ ,  $b$ ,  $c$  may depend on  $\varphi$  but the modified densities  $\zeta_\ell$  are explicitly known. Interpreting (65) as an archetype PDE (45), empowers its  $\mathcal{O}(\delta t^2)$  integration with a mixed forward/backward template

$$\varphi_i^{n+1} = \mathcal{A}_i \left( \tilde{\varphi}, \mathbf{V}^{n+1/2}, \rho^{*n}, \rho^{*n+1} \right) + \delta t \widetilde{\mathcal{R}}^\varphi|_i^{n+1} \equiv \hat{\varphi}_i + \delta t \widetilde{\mathcal{R}}^\varphi|_i^{n+1} , \quad (66)$$

where  $\widetilde{\mathcal{R}}^\varphi \equiv [\text{rhs}(65) - (b\varphi + c)]/\mathcal{G}\rho$  denotes the implicit forcing composed of the three divergence operators on the rhs of (18), while  $\tilde{\varphi} = [\varphi + \delta t(b\varphi + c)]^n$  under  $\mathcal{A}$  combines the past pressure with the explicit thermodynamic forcing in the last term on the rhs of (18). Notably, the heat source/sink  $\Pi^n$  specified in (19) and contained in  $\tilde{\varphi}$  accounts for complete forcings of full  $\theta$  and  $q_v$ , including fast and slow moist processes as well as diffusion. Altogether, the template (66) provides a discrete implicit constraint for (64), and thus for (63),

$$0 = - \sum_{\ell=1}^3 \left( \frac{A_\ell^*}{\zeta_\ell} \nabla \cdot \zeta_\ell (\check{\mathbf{v}} - \widetilde{\mathbf{G}}^T \mathbf{C} \nabla \varphi) \right) - B^*(\varphi - \hat{\varphi}) . \quad (67)$$

The coefficients  $A^*$  and  $B^*$  in (67) result from coefficients  $a_\ell$  in (65) and the superscript  $\star$  indicates that their dependence on  $\varphi$  is lagged. The Helmholtz

problem (67) was discussed in [61,31]. In NFT codes, we solve (67) with a bespoke nonsymmetric preconditioned Generalised Conjugate Residual (GCR) approach, widely discussed in the literature; cf. [58] for a recent overview and a comprehensive list of references.

#### 4.4 Spatial discretisation

The theoretical considerations and adopted formalism do not depend on modes of spatial discretisation. Namely, presentation so far applies equally well to either structured grids or unstructured meshes. In particular, the described advancements address as much the new hybrid finite-volume (FV) module FVM [62] as its established structured-grid finite-difference (FD) predecessor EULAG [38,61,32]. This versatility primarily owes to the colocated arrangement of the dependent variables, which also facilitates the advocated NFT-FV semi-implicit integrators. Because all relevant aspects of the spatial discretisation were recently expounded in [62], we refer the interested reader to that source and only briefly recall a few key generalities.

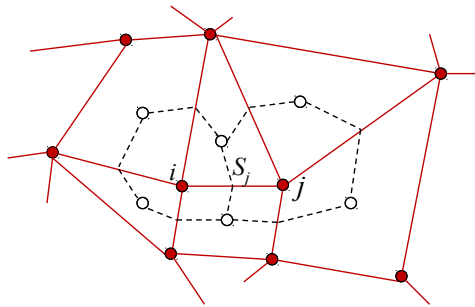


Fig. 1. An edge-based, median-dual mesh. The edge connecting nodes  $i$  and  $j$  of the primary polygonal mesh pierces, precisely in the edge centre, the face  $S_j$  shared by computational dual cells surrounding nodes  $i$  and  $j$ ; open circles represent barycentres of the primary mesh, while solid and dashed lines mark primary and dual meshes, respectively.

First, all calculations shown in the following section use a hybrid of two discretisation standards. In the horizontal, flexible fully unstructured median-dual meshes, Fig. 1, favour FV discretisations, with the components of nabla evaluated in the mesh nodes using the Gauss-divergence theorem [65–67]. In the vertical, generic second-order-accurate centred FDs are used for the nodal values of the radial partial derivative. The hybrid MPDATA judiciously combines FV and FD variants [62,29], derivable from first principles separately for the FD [45,51,52,55,28] and FV [54,65,29] modes of discretisation. As MPDATA evaluates both spatial derivatives and field values between the nodes—in the spirit of staggered grids—these evaluations are different for structured grids and unstructured meshes.

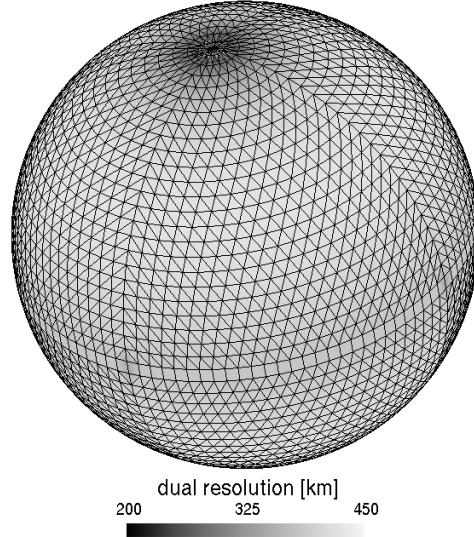


Fig. 2. Octahedral mesh O24 generated about reduced Gaussian with approximate resolution of  $3.75^\circ$  (415 km). The shading represents the dual resolution, computed as the square root of the local dual volume.

Second, although in general the numerics of FVM can use any horizontal meshing, cf. [63], our interests so far are limited to bespoke meshes with control volumes built about the Gaussian grids of the Integrated Forecasting System (IFS) of ECMWF, Fig 2. While this imposes certain constraints on mesh design [62], it accommodates both spectral-transform and grid-point solutions at the same physical locations. In return, FVM inherits the equal regions domain decomposition parallelisation scheme of the IFS, with multiple layers of parallelism hybridising MPI tasks and OpenMP threads [34,62].

## 5 RESULTS

In the following, we illustrate theoretical considerations of the preceding sections with FVM simulations of the idealised supercell thunderstorm on a 120-fold reduced-size sphere [27]. This problem captures intricate evolution of tornadic storms governed by intense vorticity dynamics and heavy precipitation [25,26]. Over the last four decades the problem has accumulated substantial literature as an epitome of complex phenomena underlying severe weather. Because it addresses a key area of nonhydrostatic dynamics and poses challenges to numerical simulation, it has recently been extended to the reduced-size planet framework of [74] for testing nonhydrostatic models, to become a standard benchmark for global model intercomparisons [27,8].

A supercell thunderstorm is a distinct atmospheric mesoscale phenomenon with a convective cloud growing throughout the depth of the troposphere,

forming a coherent structure and altering the ambient flow rather than being a mere perturbation of it. The supercell updraughts can achieve strength of hurricane winds, in contrast with turbulence normally experienced while flying through clouds characterised by vertical velocities of  $\mathcal{O}(1)$   $\text{m s}^{-1}$ . Moisture plays an essential role for the supercell formation. It provides means for the intricate hydrodynamical instabilities that condition development of deep convection as well as for enabling heavy precipitation playing a key role in the supercell evolution [26,64]. Although simpler in scope than simulation of cloud fields naturally evolving in response to diurnal cycle and intricacies of environmental forcing [46,48], a controlled simulation of the archetypal supercell evolution can be challenging. This is because large latent heat release and the associated flow response occur at the finest scales and disturb the coherence of resolved motions important for the process. Consequently, results of such simulations can be sensitive to initial/boundary conditions and details of model numerics [5,31]. Such sensitivities are typically mitigated with explicit viscosity and diffusion, aiming to assure a well-posed and numerically-resolvable problem [25,31,27].

The two characteristic ingredients of the supercell simulation are ambient conditions (wind, temperature and moisture profiles) conducive to supercells development and a smooth localised initial perturbation of ambient potential temperature; cf. Appendix C. The detailed ambient and initial conditions specified following [27] are available online at [8], including handy FORTRAN scripts and instructions. Here, we only outline alternative analytic—as opposed to standard numerical—means for extending the thermodynamic profiles specified at the equator (summarised in Appendix C for the reader’s convenience) to a balanced environment on a reduced sphere. In particular, the prescribed zonal ambient wind

$$\mathbf{u}_a(\phi, z) = [u_a(\phi, z), 0, 0] \equiv [\hat{u}(z) \cos(\phi), 0, 0], \quad (68)$$

assumes a strongly sheared equatorial wind  $\hat{u}(z)$  together with corresponding profiles of potential temperature  $\hat{\theta}(z)$  and relative humidity  $\hat{H}(z)$ . These equatorial profiles idealise a typical supercell environment. Having available  $\hat{\theta}(z)$  and  $\hat{H}(z) \equiv \hat{q}_v(z)/q_{vs}(\hat{T}, \hat{p})$  suffices to recover all necessary thermodynamic profiles assuming hydrostatic balance and using formulae of moist thermodynamics, provided in Sections 2.1.1 and 2.1.2. Furthermore, assuming the shallow atmosphere approximation in the governing PDEs (cf. Appendix B), moist undersaturated environment and the geostrophic balance (16) the analytic expressions can be derived for ambient distributions of  $\theta_{\rho a}(\phi, z)$  and Exner pressure  $\pi_a(\phi, z)$  compatible with the ambient wind (68),

$$\theta_{\rho}(\phi, z) = \hat{\theta}_{\rho}(z) \exp[\sin^2(\phi)B(z)], \quad (69a)$$

$$\pi(\phi, z) = \hat{\pi}(z) - \frac{\exp[-\sin^2(\phi)B(z)] - 1}{2c_p \hat{\theta}_{\rho} C(z)}, \quad (69b)$$

where

$$B(z) = \widehat{U}^* C(z), \quad C(z) := \frac{1}{2g} \left[ \frac{1}{\widehat{\theta}_\rho} \frac{d\widehat{\theta}_\rho}{dz} - \frac{1}{\widehat{U}^*} \frac{d\widehat{U}^*}{dz} \right], \quad (70)$$

$$\widehat{U}^*(z) := \widehat{u}^2 + a f_0 \widehat{u},$$

and  $\widehat{\cdot}$  accents denote equatorial profiles.

t [h]	$w^{\min}, w^{\max}$	$q_v^{\max}, q_c^{\max}, q_p^{\max}$	$\overline{Rq_p}, Rq_p^{\max}$	$\Delta q_t$
0	0, 0	0.014, 0, 0	0, 0	0
0.5	-9.32, 34.0	0.0157, 0.0027, 0.0141	0.03, 58.6	$-10^{-3}$
1	-21.8, 39.0	0.0161, 0.0045, 0.0136	0.46, 135	-0.27
1.5	-19.3, 45.6	0.0150, 0.0048, 0.0139	0.60, 110	-0.88
2.	-27.6, 47.9	0.0155, 0.0043, 0.0151	0.78, 129	-1.6

Table 1

Histories of vertical velocity extrema [m/s], water-species maximal mixing ratios [kg/kg], precipitation-rate means and maxima [mm/h], and total water deficit/excess [ $\pm\%$ ] defined in (71).

The sample results of a supercell simulation with FVM are summarised in Table 1 and Fig. 3. The highlighted calculations assume a 20 km deep spherical shell with 53.1 km inner radius, and a 2 h simulated time to cover the storm evolution. The shell is horizontally discretised on the O180 mesh (cf. Fig. 2) with quasi-uniform spacing  $\delta_h \lesssim 500$  m on the reduced planet. In the vertical, a regular grid is employed with uniform increment  $\delta_z = 500$  m. A variable time step is specified according to the maximal advective Courant number set at 0.97. Table 1 substantiates the earlier statements on the severity of supercell storms by showing extreme values of vertical velocities, maximal mixing ratios of the water species ( $q_p$  in particular), averaged and maximal surface precipitation rates, and the total water deficit/excess defined as

$$\Delta q_t := \left[ \int (\rho^* q_t) / \int (\rho^* q_t)^0 \right] - 1 \quad (71)$$

where the superscript 0 refers to initial fields and the integration extends over the entire model domain. Overall, the results in Table 1 and Fig. 3 verify similar compilations already presented in the literature. In particular, the updraughts maxima are consistent with the related results in Fig. 12 of [27], Fig. 6 of [31] and Fig. 11 of [5], whereas the maximal mixing ratios of cloud and precipitation water adequately agree with the results shown in the same two figures of [31] and [5]. Furthermore, Fig. 3 documents the characteristic updraught splitting in two disjoint cells past 30 min, matching a similar display in Fig. 11 of [27].

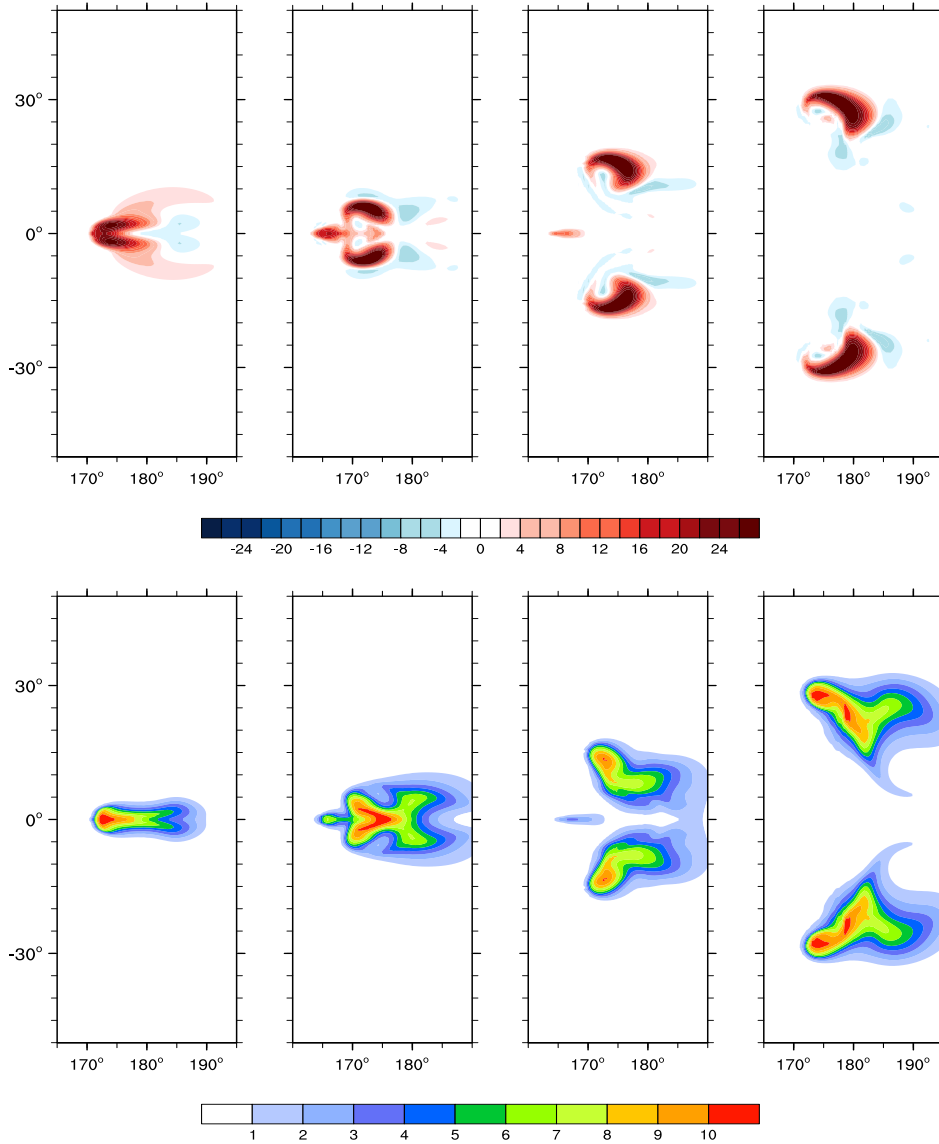


Fig. 3. The FVM supercell simulation on a reduced-size planet with horizontal spacing  $\delta_h \lesssim 500$ . Horizontal cross sections at 5 km altitude are shown in 30 min intervals for vertical velocity (top; contour interval  $2 \text{ m s}^{-1}$ ), and rainwater (bottom; contour interval  $1 \text{ g kg}^{-1}$ ).

Noteworthy are data in the last two columns of Table 1. The total loss of water substance after 2h,  $\Delta q_t = -1.6\%$  of the initial integral mass of water vapour  $1.645 \cdot 10^{12} \text{ kg}$ , can be perceived as substantial, if thought of in abstraction from the water cycle with evapotranspiration and hydrology. The current simulation employs an open boundary approximation for the precipitation fallout, and the diagnosed deficit is consistent with the mean precipitation rates,<sup>10</sup> indicating that predicted total water loss is physically meaningful rather than a numerical

<sup>10</sup> The trapezoidal approximation to the 2h integral of the  $\overline{Rq_p}$  values listed in Table 1 matches the deficit within the multiplicative factor 1.01 .

artefact. A more precise quantification of the deficit fraction due to the fallout (as opposed to truncation errors) requires evaluating the cumulative (over all simulation time steps) precipitation flux, integrated over the lower boundary of the model [17]. Because we wish to address numerical details affecting model conservativeness, we consider an analogous simulation with an impermeable boundary for the precipitation fallout that conveniently provides an alternative assessment of the conservation error.

t [h]	$w^{\min}, w^{\max}$	$q_v^{\max}, q_c^{\max}, q_p^{\max}$	$\overline{Rq_p}, Rq_p^{\max}$	$\Delta q_t$
0	0, 0	0.014, 0, 0	0, 0	0
0.5	-9.32, 34.0	0.0163, 0.0027, 0.0141	$-10^{-17}, 10^{-11}$	$-10^{-14}$
1	-21.2, 39.7	0.0161, 0.0042, 0.0446	$-10^{-9}, 10^{-11}$	$10^{-9}$
1.5	-23.4, 46.0	0.0162, 0.0045, 0.0403	$-10^{-9}, 10^{-11}$	$10^{-4}$
2	-24.8, 47.9	0.0165, 0.0041, 0.0604	$-10^{-8}, 10^{-11}$	$10^{-3}$

Table 2

As Table 1 but under the assumption of an impermeable surface for the precipitation fallout.

As substantiated in Table 2, the resulting supercell is overall similar to that highlighted in Table 1, except for huge maxima of the precipitation mixing ratios. These large values of  $q_p^{\max}$  mark the puddle formed by the fallout and washed to the lee by the surface wind, Fig. 4. Because the water collected at the ground is subject to phase changes in the same manner as aloft, it can evaporate, feed the moisture back to the system and re-enter the cloud-evolution process. Moreover, as the governing PDEs (14) account for dissipation/diffusion with constant viscosity  $\nu = 500 \text{ m}^2\text{s}^{-1}$  and Prandtl number  $Pr = 1/3$  [27], the puddle provides a reservoir for diffusion of  $q_p$  to the atmosphere, as evidenced by the water substance excess in the last column of Table 2. Albeit mathematically correct under the impermeable-surface assumption, this process is unrealistic and subject to truncation errors unaccounted for by the design of the standard benchmark. Nonetheless, the values of the water substance excess are sufficiently small to verify the thesis that the loss in Table 1 is essentially due to the precipitation fallout.

Although in relative terms the magnitude of the water-substance conservation error may appear acceptable, in absolute terms the unaccounted-for  $\Delta q_t \approx 10^{-3} \%$  translates to  $10^7$  kg of water that can be worrisome, especially in the context of climate models. To further assess the dependence of the conservation errors on details of numerics, we conducted a series of experiments with various boundary conditions for precipitation fallout and diffusion as well as a few alternative forms of enforcing positivity of water-species mixing ratios. The summary of our conclusions is guided by the results collected in Table 3.

The first and the second row of Table 3 repeat the last rows of Tables 1 and 2,

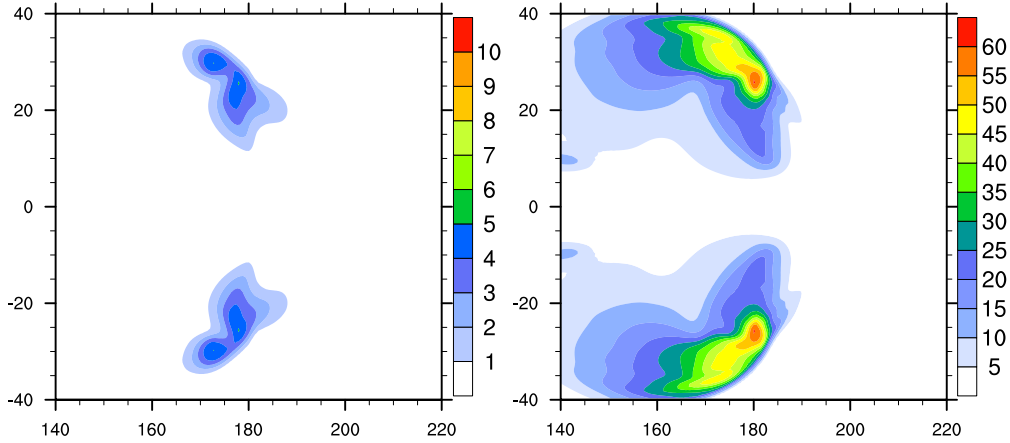


Fig. 4. Surface  $q_p$  [ $\text{gkg}^{-1}$ ] at  $t = 2$  h in two identical simulations, except for the open (run MpW0V1; left) versus impermeable (run MpW1V1; right) boundary conditions for the precipitation fallout.

run [h]	$w^{\min}, w^{\max}$	$q_v^{\max}, q_c^{\max}, q_p^{\max}$	$\overline{Rq_p}, Rq_p^{\max}$	$\Delta q_t$
MpW0V1	-27.2, 47.8	0.0155, 0.0044, 0.0151	0.78, 130	-1.6
MpW1V1	-24.8, 47.9	0.0165, 0.0041, 0.0604	$-10^{-8}, 10^{-11}$	$10^{-3}$
MgW1V1	-24.9, 48.2	0.0165, 0.0041, 0.0597	$-10^{-8}, 10^{-11}$	$10^{-3}$
MgW1V0	-25.7, 45.4	0.0172, 0.0053, 0.2738	$-10^{-17}, 10^{-11}$	$10^{-8}$
MpW1V0	-28.9, 58.1	0.0171, 0.0046, 0.1802	$-10^{-16}, 10^{-11}$	$10^{-13}$

Table 3

Vertical velocity extrema [m/s], water-species maximal mixing ratios [kg/kg], precipitation rate means and maxima [mm/h], and total water deficit/excess [ $\pm\%$ ] after 2h simulated time, for runs with various model set-ups; Mp/Mg refers to standard/infinite-gauge variants of MPDATA, W0/W1 to open/impermeable lower boundary for precipitation fallout, and V1/V0 to diffusion ON/OFF for all specific variables.

respectively. Both these runs use the afore specified dissipation, and the bespoke advection approach that applies non-oscillatory MPDATA to moist specific variables in (53) as well as to their corresponding forcings in (54), while the non-oscillatory infinite-gauge MPDATA variant (hereafter  $\text{MPDATA}_\infty$ ) is applied to all other prognostic variables, which are common to dry and moist dynamics. A comprehensive technical exposition of FV MPDATAs for arbitrary hybrid computational meshes is provided in [29]. For the purpose of this paper, the only important distinction is that the MPDATA is strictly sign-preserving (even in absence of non-oscillatory option), whereas positivity of  $\text{MPDATA}_\infty$  relies on non-oscillatory enhancement and is assured only to round-off errors. Thus, the only difference between the MpW0V1 and MpW1V1 runs is the surface boundary condition for the precipitation fallout, as discussed earlier. The run MgW1V1 parallels the MpW1V1, except that  $\text{MPDATA}_\infty$  is applied to

all advected variables, with the intent to assess the role of residual oscillations in advective transport of moist variables on the solution accuracy. Judging by the numbers collected in the second and the third row of Table 3, the two solutions are close. This is corroborated by Fig. 5 that also hints (indirectly) at a close agreement of the solution aloft in the first three runs summarised in Table 3.

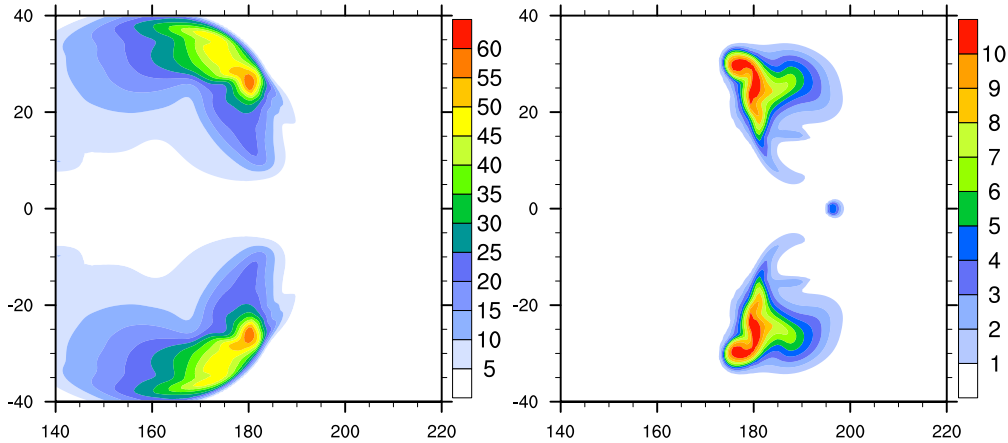


Fig. 5. Precipitation mixing ratio  $q_p$  [ $\text{g kg}^{-1}$ ] at  $t = 2$  h in the MgW1V1 simulation at the surface (left) and 5 km aloft (right). The surface solution compares with the MpW1V1 result in the right panel of Fig. 4; whereas the 5 km solution compares with the MPW0V1 result in the right-most panel of the bottom row in Fig. 3.

Having established credibility of the viscous results in the first three rows of Table 3, we now return to the water-substance conservation issue underlined in the last column of the table. The simulations MgW1V0 and MpW1V0 repeat, respectively, MgW1V1 and MpW1V1 runs with exception of setting the viscosity  $\nu \equiv 0$ . Such explicitly inviscid calculations rely on the implicit large-eddy-simulation (ILES; [22]) property of MPDATA-based high-Reynolds-number solvers, widely documented in the literature across a range of physical scenarios and scales [9,38,59–61,32,67,62]. Discarding the viscosity eliminates the unrealistic moisture supply due to the diffusion from the puddle (discussed above), and the last column of Table 3 documents the anticipated improvement of the conservation error, by 5 and 10 orders of magnitude for the  $\text{MPDATA}_\infty$  and the default MPDATA, respectively. Notably, larger conservation errors in the  $\text{MPDATA}_\infty$  run are due to the accumulation of roundoff-error negatives in the FCT flux limiting, subsequently chopped off by the limiters of the  $\mathcal{PCM}$  integrators (55) detailed in Section 3.<sup>11</sup> Insofar as the adopted solution characteristics are concerned, the inviscid results are consistent with each other and overall agree with their viscous equivalents, except for substantially stronger downdraughts and  $q_p$  maxima. The respective solutions, corresponding to the

<sup>11</sup> Recall, that considerations of Section 3 assure mathematically exact conservation of the total water substance given strict positivity of advection.

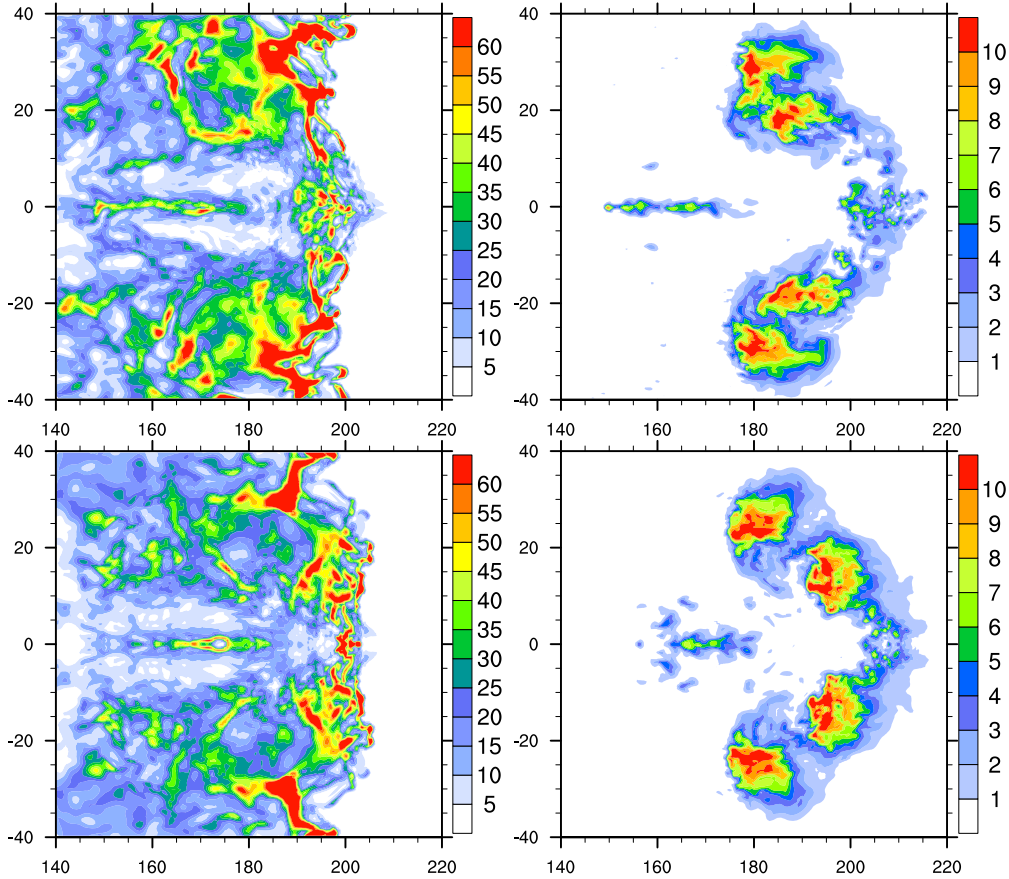


Fig. 6. As in Fig. 5 but for the inviscid runs MgW1V0 (top) and MpW1V0 (bottom).

viscous results in Fig. 5, are shown in Fig. 6. The higher Reynolds number solutions show substantially different morphology especially in small scales. Altogether, our ILES calculations corroborate results of [31] (cf. their Figs. 8-9 and the accompanying discussion), illustrate the benchmark's sensitivity to the assumed artificial viscosity and numerical details, while concomitantly attesting to the high degree of conservativeness available with FVM.

## 6 CONCLUSION

Early state-of-the-art 3D cloud models used fairly small horizontal domains  $\mathcal{O}(10^3)$  km<sup>2</sup> resolved with coarse grid spacings of  $\approx 1$  km and modest size grids not exceeding  $\sim 50^3$  nodes; cf. [25,5,46]. Nowadays, simulations of global weather and climate at  $\mathcal{O}(1)$  km horizontal mesh spacing are not only envisaged [2,36] but are already in progress [42,35,40,75]. The calculations performed with operational settings at  $\approx 1$  km horizontal mesh spacing, highlighted in [40,75], attest to the tremendous advancement of computational meteorology over the last four decades. It is this advancement that extends the relevance of bulk microphysics parametrisations, originated for research

of cloud dynamics and physics, to global weather and climate models; see [44,43,76] for recent substantive developments and pertinent discussions. Historically, such models had to rely on sophisticated diagnostic subgrid-scale parametrisation schemes [69], only recently superseded with more advanced prognostic bulk microphysics [11]. The particular approach adopted for this paper [13,14] assumes canonical warm-rain microphysics at the core of convective cloud models. Albeit physically simple, it contains the essential numerical ingredients for generalisation to an all-scale method [15–17,31,32]. While the underlying ideas were presented in application papers, its actual mathematical apparatus and numerical machinery have never been documented in comprehensive detail. The current paper fills this gap, while extending the whole concept to integration on manifolds using flexible finite-volume (FV) discretisations on arbitrary hybrid computational meshes.

The PDEs describing evolution of water species in bulk microphysics parametrisations take a form of the generalised transport equation (45) with the right-hand-side dependent on variables representing all water species as well as the thermodynamic state of the system. While the lhs of (45) is analytically expressed in the flux form, and thus susceptible to conservative FV discretisation, the dependencies on the rhs include transcendental functions and power laws that assure conservation of the sum of all species—i.e., the total water substance—subject to the boundary conditions for the precipitation fallout. In consequence, designing a model conserving water substance to machine precision entails judicious design of the rhs integrals. The design presented in this paper exploits positivity of all water species and thus benefits from sign-preservation of dependent variables in the advective transport. The results of Section 5 show that not all means of assuring the positivity of advection are equal. In that the standard MPDATA, attaining strict positivity based on the convexity of upwinding, provides superior results to the infinite-gauge MPDATA, attaining a round-off error positivity based on the FCT limiting. This emphasises the role of algorithm customisation in addressing the behavioural errors; cf. §III-A-23 in [41]. Namely, the standard MPDATA deliberately targets the transport of water species in cloud models [45,47,49], while the infinite-gauge variant targets the transport of fields with variable sign [52,54,29]—even though both can transport arbitrary fields to second-order accuracy.

The numerical approximations specific to the microphysics parametrisation and their coupling to the semi-implicit integrators for the all-scale dynamics were substantiated with a select problem of severe mesoscale weather. A tornadic thunderstorm simulation benchmark [25], recently adopted to a reduced size planet [27], is highly sensitive to the imposed viscosity and numerical details [31] and thereby serves well as a discriminating example. In particular, a focused series of numerical experiments with varying model set-ups illustrates the complexity of assessing the model conservativeness, the assurance of which

spreads over several layers of the model numerics—from algorithms for advection and the rhs forcings, to compatible boundary conditions for the vector differential operators ubiquitous in the model [53]. The discussed benchmark fulfils its purpose in the context of the current paper. The reader interested in other benchmarks and relative performance of FVM compared to other models is referred to [8] and the publications to follow the program.

*Acknowledgements:* Personal review by Nils Wedi is gratefully acknowledged. Comments from Rupert Klein and an anonymous referee helped to improve the presentation. This work was supported in part by funding received from the European Research Council under the European Union’s Seventh Framework Programme (FP7/2012/ERC Grant agreement no. 320375).

## Appendix A. Microphysical formulae

In a popular “warm rain” parametrisation [25,14], the power law expressing precipitation terminal velocity in function of the dry air density and the precipitation mixing ratio can be written after [25] as

$$\vartheta(\rho, q_p) = 36.34(10^{-3}\rho q_p)^{0.1364}(\rho/\rho_0)^{-1/2}, \quad (72)$$

where the the numeral coefficients assume SI units of  $\rho$  and  $\vartheta$  [14].

Similarly, moist thermodynamic sinks and sources on the rhs of (1c)-(1f) are:

$$A_p = \max(0., k_1(q_c - q_c^T)), \quad (73)$$

$$C_p = k_2 q_c q_p^{0.875}, \quad (74)$$

$$E_p = \frac{1}{\rho} \frac{(q_v/q_{vs} - 1) C (10^{-3}\rho q_p)^{0.525}}{5.4 \times 10^2 + 2.55 \times 10^5 / (p q_{vs})}, \quad (75)$$

where  $k_1 = 10^{-3} \text{ s}^{-1}$ , the autoconversion threshold  $q_c^T$  depends on a particular application but typically is between  $10^{-4}$  and  $10^{-3} \text{ kg kg}^{-1}$ ,  $k_2 = 2.2 \text{ s}^{-1}$ , and  $C = 1.6 + 124.9(10^{-3}\rho q_p)^{0.2046}$  is the ventilation factor.

## Appendix B. Specifications of the spherical frame

In the spherical curvilinear framework of [37], the vector  $\mathbf{u}$  represents the physical velocity with components aligned at every point of the spherical shell with axes of a local Cartesian frame (subsequently marked as  $_c$ ) tangent to the lower surface ( $r = a$ ) of the shell;  $r$  is the radial component of the vector radius,

and  $a$  is the radius of the sphere, cf. Fig. 7.7, section 7.2 in [10]. Consequently,  $dx_c = r \cos \phi d\lambda$ ,  $dy_c = r d\phi$  and  $z_c = r - a$ ; where  $\lambda$  and  $\phi$  denote longitude and latitude angles, respectively. Then, in the formalism of Sections 2 and 4 and in the absence of coordinate stretching,  $x = a\lambda$ ,  $y = a\phi$ , and  $z = z_c$ ; thereby effectively employing longitude-latitude coordinates standard in many global atmospheric models [66]. Furthermore, the coefficient matrix  $\widetilde{\mathbf{G}}$  consists of zero off-diagonal entries, whereas  $\widetilde{G}_1^1 = [\Gamma \cos(y/a)]^{-1}$ ,  $\widetilde{G}_2^2 = \Gamma^{-1}$ , and  $\widetilde{G}_3^3 = 1$ . Here,  $\Gamma = 1 + \chi z/a$ , and indices 1, 2, and 3 correspond to  $x$ ,  $y$ , and  $z$  components. Consequently, the Jacobian is  $\mathcal{G} = \Gamma^2 \cos(y/a)$ . The parameter  $\chi$  is set to unity by default; whereas the optional setting  $\chi = 0$  selects the shallow atmosphere approximation in the governing PDEs [74].

In the momentum equation, the components of the Coriolis acceleration are

$$-\mathbf{f} \times \mathbf{u} = \begin{bmatrix} v f_0 \sin(y/a) - \chi w f_0 \cos(y/a), \\ -u f_0 \sin(y/a), \\ \chi u f_0 \cos(y/a) \end{bmatrix}, \quad (76)$$

where  $\mathbf{u} = [u, v, w]$  and  $f_0 = 2|\boldsymbol{\Omega}|$ . Furthermore, the metric forcings (viz., component-wise Christoffel terms associated with the convective derivative of the physical velocity) are,

$$\mathcal{M}(\mathbf{u}) = (\Gamma a)^{-1} \begin{bmatrix} \tan(y/a) u v - \chi u w, \\ -\tan(y/a) u u - \chi v w, \\ \chi (u u + v v) \end{bmatrix}. \quad (77)$$

## Appendix C. Specifications for the supercell simulation

The equatorial profile of the zonal velocity component,

$$\hat{u}(z) = \begin{cases} U_s \check{z} - U_c & \text{for } \check{z} < 0.8 \\ U_s(-1.25 \check{z}^2 + 3 \check{z} - 0.8) - U_c & \text{for } |\check{z} - 1| < 0.2 \\ U_s - U_c & \text{for } \check{z} > 1.2, \end{cases} \quad (78)$$

idealises a supercell storm environment. Here  $\check{z} := z/z_s$  with  $z_s = 5 \cdot 10^3 \text{m}$  marking the shear depth, while  $U_s = 30 \text{ms}^{-1}$  and  $U_c = 15 \text{ms}^{-1}$  are assumed. Notably, the specified  $U_c$  is a numerical facilitator with an interpretation of a Galilean shift, placing the observer in the reference frame of the moving storm

[27]. The equatorial potential temperature is accordingly prescribed as

$$\hat{\theta}(z) = \begin{cases} \theta_0 + (\theta_{tr} - \theta_0) \check{z}^{1.25} & \text{for } \check{z} \leq 1 \\ \theta_{tr} \exp[S(z - z_{tr})] & \text{for } \check{z} > 1. \end{cases} \quad (79)$$

Here  $\check{z} := z/z_{tr}$ ,  $z_{tr} = 12 \cdot 10^3$  m denotes the height of the tropopause, the stratification  $S = g/(c_p T_{tr})$ , and  $T_{tr} = 213$  K marks the temperature of the isothermal stratosphere. Furthermore, the relative humidity profile is defined as

$$\widehat{H}(z) = \begin{cases} 1 - 0.75 \check{z}^{1.25} & \text{for } \check{z} \leq 1 \\ 0.25 & \text{for } \check{z} > 1. \end{cases} \quad (80)$$

A smooth spheroidal perturbation  $\delta\theta(\lambda, \phi, z)$ —added to the ambient field  $\theta(\phi, z)$  to initiate convection—is specified according to

$$\delta\theta = \begin{cases} \Delta\theta \cos^2(0.5\pi R_\theta) & \text{for } R_\theta < 1 \\ 0 & \text{for } R_\theta \geq 1, \end{cases} \quad (81)$$

where

$$R_\theta = \left[ \left( r(\lambda, \phi)/r_h \right)^2 + \left( (z - z_c)/r_z \right)^2 \right]^{1/2}. \quad (82)$$

Here,  $r(\lambda, \phi)$  denotes the great-circle distance from the perturbation's origin, the spheroid dimension parameters  $r_h$  and  $r_z$  are 10 and 1.5 km, respectively, and the magnitude of the perturbation  $\Delta\theta = 3$  K is assumed.

## References

- [1] M. Andrejczuk, W.W. Grabowski, S.P. Malinowski, P.K. Smolarkiewicz, Numerical simulation of cloud-clear air interfacial mixing, *J. Atmos. Sci.*, 61 (2004) 1726–1739.
- [2] P. Bauer, A. Thorpe, G. Brunet, The quiet revolution of numerical weather prediction, *Nature* 525 (2015) 47–55.
- [3] G.H. Bryan, J.M. Fritsch, A benchmark simulation for moist nonhydrostatic numerical models, *Mon. Weather Rev.* 130 (2002) 2917–2928.
- [4] P.S. Brown, An implicit scheme for efficient solution of the coalescence/collision-breakup equation, *J. Comput. Phys.* 58 (1985) 417–431.
- [5] T.L. Clark, Numerical simulations with three-dimensional cloud model: Lateral boundary condition experiments and multicellular severe storm simulations, *J. Atmos. Sci.* 36 (1979) 2191–2215.

- [6] J.F. Cossette, P.K. Smolarkiewicz, P. Charbonneau, The Monge-Ampère trajectory correction for semi-Lagrangian schemes, *J. Comput. Phys.* 274 (2014) 208–229.
- [7] R. Courant, D. Hilbert, *Methods of Mathematical Physics*, vol. 2, Wiley Classics Edition, 1989, pp. 830.
- [8] <https://github.com/ClimateGlobalChange/DCMIP2016>
- [9] J.A. Domaradzki, Z. Xiao, P.K. Smolarkiewicz, Effective eddy viscosities in implicit large eddy simulations of turbulent flows, *Phys. Fluids* 15 (2003) 3890–3893.
- [10] J.A. Dutton, *The Ceaseless Wind*. Dover Publications, 1986, pp. 617.
- [11] R.M. Forbes, A.M. Tompkins, A. Untch, A new prognostic microphysics scheme for the IFS, Technical Memorandum 649 (2011), ECMWF, pp. 28.
- [12] R.M. Forbes, M. Ahlgrim, On the representation of high-latitude boundary layer mixed-phase cloud in the ECMWF global model, *Mon. Weather Rev.* 142 (2014) 3425–3435.
- [13] W.W. Grabowski, P.K. Smolarkiewicz, Monotone finite-difference approximations to the advection-condensation problem, *Mon. Weather Rev.* 118 (1990), 2082–2097.
- [14] W.W. Grabowski, P.K. Smolarkiewicz, Two-time-level semi-Lagrangian modeling of precipitating clouds, *Mon. Weather Rev.* 124 (1996) 487–497.
- [15] W.W. Grabowski, Toward cloud resolving modeling of large-scale tropical convections: A simple cloud microphysics parameterization, *J. Atmos. Sci.*, 55 (1998) 3283–3298.
- [16] W.W. Grabowski, A parameterization of cloud microphysics for long-term cloud-resolving modeling of tropical convection, *Atmos. Research* 52 (1999) 17–41.
- [17] W.W. Grabowski, P.K. Smolarkiewicz, A multiscale anelastic model for meteorological research, *Mon. Weather Rev.*, 130 (2002), 939–956.
- [18] W.W. Grabowski, L.P. Wang, Growth of cloud droplets in a turbulent environment, *Annu. Rev. Fluid Mech.*, 45 (2013), 293–324.
- [19] W.W. Grabowski, Untangling microphysical impacts on deep convection applying novel modeling methodology, *J. Atmos. Sci.*, 72 (2015) 2446–2464.
- [20] W.W. Grabowski, D. Jarecka, Modeling condensation in shallow nonprecipitating convection, *J. Atmos. Sci.*, 72 (2015) 4661–4679.
- [21] W.W. Grabowski, H. Morrison, Untangling microphysical impacts on deep convection applying a novel modeling methodology. Part II: Double-moment, *J. Atmos. Sci.*, 73 (2016) 3749–3770.

- [22] F.F. Grinstein, L. Margolin, W. Rider, *Implicit Large Eddy Simulation: Computing Turbulent Fluid Dynamics*, Cambridge University Press (2007) pp 546.
- [23] A. Khain, M. Ovtchinnikov, M. Pinsky, A. Pokrovsky, H. Krugliak (2000), Notes on the state-of-the-art numerical modeling of cloud microphysics, *Atmos. Research*, 55 (2010) 159–224.
- [24] R. Klein, Scale-dependent models for atmospheric flows. *Ann. Rev. Fluid Mech.* 42 (2010) 249–274.
- [25] J.B. Klemp, R.B. Wilhelmson, The simulation of three-dimensional convective storm dynamics, *J. Atmos. Sci.* 35 (1978) 1070–1096.
- [26] J.B. Klemp, Dynamics of tornadic thunderstorms, *Ann. Rev. Fluid Mech.* 19 (1987) 369–402.
- [27] J.B. Klemp, W.C. Skamarock, S.-H. Park, Idealized global nonhydrostatic atmospheric test cases on a reduced-radius sphere, *J. Adv. Model. Earth. Syst.* 7 (2015) 1155–1177.
- [28] C. Kühnlein, P.K. Smolarkiewicz, A. Dörnbrack, Modelling atmospheric flows with adaptive moving meshes, *J. Comput. Phys.* 231 (2012) 2741–2763.
- [29] C. Kühnlein, P.K. Smolarkiewicz, An unstructured-mesh finite-volume MPDATA for compressible atmospheric dynamics, *J. Comput. Phys.* 334 (2017) 16–30.
- [30] M.J. Kurowski, W.W. Grabowski, and P.K. Smolarkiewicz, Toward multiscale simulation of moist flows with soundproof equations, *J. Atmos. Sci.* 70 (2013) 3995–4011.
- [31] M.J. Kurowski, W.W. Grabowski, and P.K. Smolarkiewicz, Anelastic and compressible simulations of moist deep convection, *J. Atmos. Sci.* 71 (2014) 3767–3787.
- [32] M.J. Kurowski, W.W. Grabowski, and P.K. Smolarkiewicz, Anelastic and compressible simulations of moist dynamics at planetary scales, *J. Atmos. Sci.* 72 (2015) 3975–3995.
- [33] P. Marquet, Definition of a moist entropy potential temperature: application to FIRE-I data flights, *Q.J. Roy. Meteorol. Soc.*, 137 (2011) 768–791.
- [34] G. Mozdzyński, M. Hamrud, N.P. Wedi (2015), A partitioned global address space implementation of the ECMWF Integrated Forecasting System (IFS), *Int. J. High Perform. C.* 29 (2015) 261–273.
- [35] Y. Miyamoto, Y. Kajikawa, R. Ypshida, T. Yamaura, Y. Yashiro, H. Tomita, Deep moist atmospheric convection in a subkilometer global simulation, *Geophys. Res. Lett.* 40 (2013) 4922–4926.
- [36] T. Palmer, Build high-resolution global climate models, *Nature* 515 (2014) 338–339.

- [37] J.M. Prusa, P.K. Smolarkiewicz, An all-scale anelastic model for geophysical flows: dynamic grid deformation, *J. Comput. Phys.* 190 (2003) 601–622.
- [38] J.M. Prusa, P.K. Smolarkiewicz, A.A Wyszogrodzki, EULAG, a computational model for multiscale flows, *Comput. Fluids* 37 (2008) 1193–1207
- [39] H.R. Pruppacher, J.D. Klett, *Microphysics of Clouds and Precipitation*, Dordrecht: Kluwer Acad. 1997, pp. 954.
- [40] W. Putman, Scaling the software and advancing the science of global modeling and assimilation systems at NASA, 17th Workshop on High Performance Computing in Meteorology, ECMWF, Reading 24-28 October 2016, <http://www.ecmwf.int/en/learning/workshops-and-seminars/17th-workshop-high-performance-computing-meteorology>
- [41] P.J. Roache, *Computational Fluid Dynamics*, Hermosa Publishers, 1972, pp. 434.
- [42] M. Satoh, T. Matsuno, H. Tomita, H. Miura, T. Nasuno, S. Iga, Nonhydrostatic icosahedral atmospheric model (NICAM) for global cloud resolving simulations, *J. Comput. Phys.* 227 (2008) 3486–3514.
- [43] M. Satoh, H. Tomita, H. Yashiro, H. Miura, C. Kodama, T. Seiki, A.T. Noda, Y. Yamada, D. Goto, M. Sawada, T. Miyoshi, Y. Niwa, M. Hara, T. Ohno, S. Iga, T. Arakawa, T. Inoue, H. Kubokawa, The non-hydrostatic icosahedral atmospheric model: description and development, *Prog. Earth Planet Sci.* 1:18 (2014) 1–32.
- [44] W.C. Skamarock, J.B. Klemp, M.G. Duda, L.D. Fowler, S.-H. Park, T.D. Ringler, A multiscale nonhydrostatic atmospheric model using centroidal Voronoi tessellations and C-grid staggering, *Month. Weather Rev.* 140 (2012) 3090–3105.
- [45] P.K. Smolarkiewicz, A fully multidimensional positive definite advection transport algorithm with small implicit diffusion, *J. Comput. Phys.*, 54 (1984) 325–362.
- [46] P.K. Smolarkiewicz, T.L. Clark, Numerical-simulation of the evolution of a 3-dimensional field of cumulus clouds. Part I: Model description, comparison with observations and sensitivity studies, *J. Atmos. Sci.* 42 (1985) 502–522.
- [47] P.K. Smolarkiewicz, T.L. Clark, The multidimensional positive definite advection transport algorithm; Further developments and applications, *J. Comput. Phys.*, 67 (1986) 396–438.
- [48] P.K. Smolarkiewicz, R.M. Rasmussen, T.L. Clark, On the dynamics of Hawaiian cloud bands: island forcing, *J. Atmos. Sci.* 45 (1988) 1872–1905.
- [49] P.K. Smolarkiewicz, W.W. Grabowski: The multidimensional positive definite advection transport algorithm: nonoscillatory option, *J. Comput. Phys.*, 86 (1990) 355–375.
- [50] P.K. Smolarkiewicz, J.A. Pudykiewicz, A class of semi- Lagrangian approximations for fluids, *J. Atmos. Sci.* 49 (1992), 2082–2096.

- [51] P.K. Smolarkiewicz, L.G. Margolin, On forward-in-time differencing for fluids: extension to a curvilinear framework, *Mon. Weather Rev.* 121 (1993) 1847–1859.
- [52] P.K. Smolarkiewicz, L.G. Margolin, MPDATA: A finite-difference solver for geophysical flows, *J. Comput. Phys.* 140 (1998) 459–480.
- [53] P.K. Smolarkiewicz, J.A. Prusa, Towards mesh adaptivity for geophysical turbulence: continuous mapping approach, *Int. J. Numer. Meth. Fluids* 47 (2005) 789–801.
- [54] P.K. Smolarkiewicz, J. Szmelter, MPDATA: An edge-based unstructured-grid formulation, *J. Comput. Phys.* 206 (2005) 624–649.
- [55] P.K. Smolarkiewicz, Multidimensional positive definite advection transport algorithm: an overview, *Int. J. Numer. Meth. Fluids* 50 (2006) 1123–1144.
- [56] P.K. Smolarkiewicz, R. Sharman, J. Weil, S.G. Perry, D. Heist, and G. Bowker, Building resolving large-eddy simulations and comparison with wind tunnel experiments, *J. Comput. Phys.* 227 (2007) 633–653.
- [57] P.K. Smolarkiewicz, J. Szmelter, Iterated upwind schemes for gas dynamics, *J. Comput. Phys.* 228 (2009) 33–54.
- [58] P.K. Smolarkiewicz, J. Szmelter, A nonhydrostatic unstructured-mesh soundproof model for simulation of internal gravity waves, *Acta Geophysica* 59 (2011) 1109–1134.
- [59] P.K. Smolarkiewicz, P. Charbonneau, EULAG, a computational model for multiscale flows: An MHD extension, *J. Comput. Phys.* 236 (2013) 608–623.
- [60] P.K. Smolarkiewicz, J. Szmelter, A.A. Wyszogrodzki, An unstructured-mesh atmospheric model for nonhydrostatic dynamics, *J. Comput. Phys.* 254 (2013) 184–199.
- [61] P.K. Smolarkiewicz, C. Kühnlein, N.P. Wedi, A consistent framework for discrete integrations of soundproof and compressible PDEs of atmospheric dynamics, *J. Comput. Phys.* 263 (2014) 185–205
- [62] P.K. Smolarkiewicz, W. Deconinck, M. Hamrud, C. Kühnlein, G. Mozdzyński, J. Szmelter, N.P. Wedi, A finite-volume module for simulating global all-scale atmospheric flows, *J. Comput. Phys.* 315 (2016) 287–304.
- [63] P.K. Smolarkiewicz, J. Szmelter, F. Xiao, Simulation of all-scale dynamics on unstructured meshes, *J. Comput. Phys.* 322 (2016) 267–287.
- [64] B. Stevens, Atmospheric moist convection, *Annu. Rev. Earth Planet. Sci.* 33 (2005) 605–643.
- [65] J. Szmelter, P.K. Smolarkiewicz, MPDATA error estimator for mesh adaptivity, *Int. J. Numer. Meth. Fluids* 50 (2006) 1269–1293.
- [66] J. Szmelter, P.K. Smolarkiewicz, An edge-based unstructured mesh discretisation in geospherical framework, *J. Comput. Phys.* 229 (2010) 4980–4995.

- [67] J. Szmelter, Z. Zhang, P.K. Smolarkiewicz: An unstructured-mesh atmospheric model for nonhydrostatic dynamics: Towards optimal mesh resolution. *J. Comput. Phys.*, 294 (2015), 363–381.
- [68] J.M. Straka, *Cloud and precipitation microphysics — principles and parameterizations*. Cambridge University Press 2009, pp. 384.
- [69] M. Tiedtke, Representation of clouds in large-scale models, *Mon. Weather Rev.* 121 (1931) 3040–3061.
- [70] C.J. Tremback, J. Powell, W.R. Cotton, R.A. Pielke, The forward-in-time upstream advection scheme: Extension to higher orders, *Month. Weather Rev.* 115 (1987) 540-555.
- [71] G.J. Tripoli, W.R. Cotton, The use of ice-liquid water potential temperature as a thermodynamic variable in deep atmospheric models, *Mon. Weather Rev.* 109 (1981) 1094–1102.
- [72] U. Wacker, T. Frisius, F. Herbert, Evaporation and precipitation surface effects in local mass continuity laws of moist air, *J. Atmos. Sci.* 63 (2006) 2642–2652.
- [73] N.P. Wedi, P.K. Smolarkiewicz, Extending Gal-Chen and Somerville terrain-following coordinate transformation on time dependent curvilinear boundaries, *J. Comput. Phys.* 193 (2004) 1–20.
- [74] N.P. Wedi, P.K. Smolarkiewicz, A framework for testing global nonhydrostatic models, *Q.J. Roy. Meteorol. Soc.*, 135 (2009) 469–484.
- [75] N.P. Wedi, The evolving state-of-the-art in global numerical weather prediction, 17th Workshop on High Performance Computing in Meteorology, ECMWF, Reading 24-28 October 2016, <http://www.ecmwf.int/en/learning/workshops-and-seminars/17th-workshop-high-performance-computing-meteorology>
- [76] G. Zängl, D. Reinert, P. Ripodas, M. Baldauf, The ICON (ICOsahedral Non-hydrostatic) modeling framework of DWD and MPI-M: Description of the non-hydrostatic dynamical core, *Q.J. Roy. Meteorol. Soc.*, 141 (2015) 563–579.